EUROPEAN ORGANIZATION FOR NUCLEAR RESEARCH

CERN–PH-EP/2006-022

19 June 2006/rev. 7 June 2007

$Z\gamma^*$ production in e^+e^- interactions at $\sqrt{s} = 183 - 209$ GeV

DELPHI Collaboration

Abstract

Measurements of $Z\gamma^*$ production are presented using data collected by the DELPHI detector at centre-of-mass energies ranging from 183 to 209 GeV, corresponding to an integrated luminosity of about 667 pb^{-1}. The measurements cover a wide range of the possible final state four-fermion configurations: hadronic and leptonic ($e^+e^-q\bar{q}$, $\mu^+\mu^-q\bar{q}$, $q\bar{q}\nu\bar{\nu}$), fully leptonic ($l^+l^-l'^+l'^-$) and fully hadronic final states ($q\bar{q}q\bar{q}$, with a low mass $q\bar{q}$ pair). Measurements of the $Z\gamma^*$ cross-section for the various final states have been compared with the Standard Model expectations and found to be consistent within the errors. In addition, a total cross-section measurement of the $l^+l^-l'^+l'^-$ cross-section is reported, and found to be in agreement with the prediction of the Standard Model.

(Accepted by Eur. Phys. J. C)

J.Abdallah[26], P.Abreu[23], W.Adam[55], P.Adzic[12], T.Albrecht[18], R.Alemany-Fernandez[9], T.Allmendinger[18], P.P.Allport[24], U.Amaldi[30], N.Amapane[48], S.Amato[52], E.Anashkin[37], A.Andreazza[29], S.Andringa[23], N.Anjos[23], P.Antilogus[26], W-D.Apel[18], Y.Arnoud[15], S.Ask[9], B.Asman[47], J.E.Augustin[26], A.Augustinus[9], P.Baillon[9], A.Ballestrero[49], P.Bambade[21], R.Barbier[28], D.Bardin[17], G.J.Barker[57], A.Baroncelli[40], M.Battaglia[9], M.Baubillier[26], K-H.Becks[58], M.Begalli[7], A.Behrmann[58], E.Ben-Haim[21], N.Benekos[33], A.Benvenuti[5], C.Berat[15], M.Berggren[26], D.Bertrand[2], M.Besancon[41], N.Besson[41], D.Bloch[10], M.Blom[32], M.Bluj[56], M.Bonesini[30], M.Boonekamp[41], P.S.L.Booth†[24], G.Borisov[22], O.Botner[53], B.Bouquet[21], T.J.V.Bowcock[24], I.Boyko[17], M.Bracko[44], R.Brenner[53], E.Brodet[36], P.Bruckman[19], J.M.Brunet[8], B.Buschbeck[55], P.Buschmann[58], M.Calvi[30], T.Camporesi[9], V.Canale[39], F.Carena[9], N.Castro[23], F.Cavallo[5], M.Chapkin[43], Ph.Charpentier[9], P.Checchia[37], R.Chierici[9], P.Chliapnikov[43], J.Chudoba[9], S.U.Chung[9], K.Cieslik[19], P.Collins[9], R.Contri[14], G.Cosme[21], F.Cossutti[50], M.J.Costa[54], D.Crennell[38], J.Cuevas[35], J.D'Hondt[2], T.da Silva[52], W.Da Silva[26], G.Della Ricca[50], A.De Angelis[51], W.De Boer[18], C.De Clercq[2], B.De Lotto[51], N.De Maria[48], A.De Min[37], L.de Paula[52], L.Di Ciaccio[39], A.Di Simone[40], K.Doroba[56], J.Drees[58,9], G.Eigen[4], T.Ekelof[53], M.Ellert[53], M.Elsing[9], M.C.Espirito Santo[23], G.Fanourakis[12], D.Fassouliotis[12,3], M.Feindt[18], J.Fernandez[42], A.Ferrer[54], F.Ferro[14], U.Flagmeyer[58], H.Foeth[9], E.Fokitis[33], F.Fulda-Quenzer[21], J.Fuster[54], M.Gandelman[52], C.Garcia[54], Ph.Gavillet[9], E.Gazis[33], R.Gokieli[9,56], B.Golob[44,46], G.Gomez-Ceballos[42], P.Goncalves[23], E.Graziani[40], G.Grosdidier[21], K.Grzelak[56], J.Guy[38], C.Haag[18], A.Hallgren[53], K.Hamacher[58], K.Hamilton[36], S.Haug[34], F.Hauler[18], V.Hedberg[27], M.Hennecke[18], H.Herr†[9], J.Hoffman[56], S-O.Holmgren[47], P.J.Holt[9], M.A.Houlden[24], J.N.Jackson[24], G.Jarlskog[27], P.Jarry[41], D.Jeans[36], E.K.Johansson[47], P.Jonsson[28], C.Joram[9], L.Jungermann[18], F.Kapusta[26], S.Katsanevas[28], E.Katsoufis[33], G.Kernel[44], B.P.Kersevan[44,46], U.Kerzel[18], B.T.King[24], N.J.Kjaer[9], P.Kluit[32], P.Kokkinias[12], C.Kourkoumelis[3], O.Kouznetsov[17], Z.Krumstein[17], M.Kucharczyk[19], J.Lamsa[1], G.Leder[55], F.Ledroit[15], L.Leinonen[47], R.Leitner[31], J.Lemonne[2], V.Lepeltier[21], T.Lesiak[19], W.Liebig[58], D.Liko[55], A.Lipniacka[47], J.H.Lopes[52], J.M.Lopez[35], D.Loukas[12], P.Lutz[41], L.Lyons[36], J.MacNaughton[55], A.Malek[58], S.Maltezos[33], F.Mandl[55], J.Marco[42], R.Marco[42], B.Marechal[52], M.Margoni[37], J-C.Marin[9], C.Mariotti[9], A.Markou[12], C.Martinez-Rivero[42], J.Masik[13], N.Mastroyiannopoulos[12], F.Matorras[42], C.Matteuzzi[30], F.Mazzucato[37], M.Mazzucato[37], R.Mc Nulty[24], C.Meroni[29], E.Migliore[48], W.Mitaroff[55], U.Mjoernmark[27], T.Moa[47], M.Moch[18], K.Moenig[9,11], R.Monge[14], J.Montenegro[32], D.Moraes[52], S.Moreno[23], P.Morettini[14], U.Mueller[58], K.Muenich[58], M.Mulders[32], L.Mundim[7], W.Murray[38], B.Muryn[20], G.Myatt[36], T.Myklebust[34], M.Nassiakou[12], F.Navarria[5], K.Nawrocki[56], R.Nicolaidou[41], M.Nikolenko[17,10], A.Oblakowska-Mucha[20], V.Obraztsov[43], A.Olshevski[17], A.Onofre[23], R.Orava[16], K.Osterberg[16], A.Ouraou[41], A.Oyanguren[54], M.Paganoni[30], S.Paiano[5], J.P.Palacios[24], H.Palka[19], Th.D.Papadopoulou[33], L.Pape[9], C.Parkes[25], F.Parodi[14], U.Parzefall[9], A.Passeri[40], O.Passon[58], L.Peralta[23], V.Perepelitsa[54], A.Perrotta[5], A.Petrolini[14], J.Piedra[42], L.Pieri[40], F.Pierre[41], M.Pimenta[23], E.Piotto[9], T.Podobnik[44,46], V.Poireau[9], M.E.Pol[6], G.Polok[19], V.Pozdniakov[17], N.Pukhaeva[17], A.Pullia[30], J.Rames[13], A.Read[34], P.Rebecchi[9], J.Rehn[18], D.Reid[32], R.Reinhardt[58], P.Renton[36], F.Richard[21], J.Ridky[13], M.Rivero[42], D.Rodriguez[42], A.Romero[48], P.Ronchese[37], P.Roudeau[21], T.Rovelli[5], V.Ruhlmann-Kleider[41], D.Ryabtchikov[43], A.Sadovsky[17], L.Salmi[16], J.Salt[54], C.Sander[18], A.Savoy-Navarro[26], U.Schwickerath[9], R.Sekulin[38], M.Siebel[58], A.Sisakian[17], G.Smadja[28], O.Smirnova[27], A.Sokolov[43], A.Sopczak[22], R.Sosnowski[56], T.Spassov[9], M.Stanitzki[18], A.Stocchi[21], J.Strauss[55], B.Stugu[4], M.Szczekowski[56], M.Szeptycka[56], T.Szumlak[20], T.Tabarelli[30], F.Tegenfeldt[53], J.Timmermans[32], L.Tkatchev[17], M.Tobin[24], S.Todorovova[13], B.Tome[23], A.Tonazzo[30], P.Tortosa[54], P.Travnicek[13], D.Treille[9], G.Tristram[8], M.Trochimczuk[56], C.Troncon[29], M-L.Turluer[41], I.A.Tyapkin[17], P.Tyapkin[17], S.Tzamarias[12], V.Uvarov[43], G.Valenti[5], P.Van Dam[32], J.Van Eldik[9], N.van Remortel[16], I.Van Vulpen[9], G.Vegni[29], F.Veloso[23], W.Venus[38], P.Verdier[28], V.Verzi[39], D.Vilanova[41], L.Vitale[50], V.Vrba[13], H.Wahlen[58], A.J.Washbrook[24], C.Weiser[18], D.Wicke[9], J.Wickens[2], G.Wilkinson[36], M.Winter[10], M.Witek[19], O.Yushchenko[43], A.Zalewska[19], P.Zalewski[56], D.Zavrtanik[45], V.Zhuravlov[17], N.I.Zimin[17], A.Zintchenko[17], M.Zupan[12]

[1]Department of Physics and Astronomy, Iowa State University, Ames IA 50011-3160, USA
[2]IIHE, ULB-VUB, Pleinlaan 2, B-1050 Brussels, Belgium
[3]Physics Laboratory, University of Athens, Solonos Str. 104, GR-10680 Athens, Greece
[4]Department of Physics, University of Bergen, Allégaten 55, NO-5007 Bergen, Norway
[5]Dipartimento di Fisica, Università di Bologna and INFN, Via Irnerio 46, IT-40126 Bologna, Italy
[6]Centro Brasileiro de Pesquisas Físicas, rua Xavier Sigaud 150, BR-22290 Rio de Janeiro, Brazil
[7]Inst. de Física, Univ. Estadual do Rio de Janeiro, rua São Francisco Xavier 524, Rio de Janeiro, Brazil
[8]Collège de France, Lab. de Physique Corpusculaire, IN2P3-CNRS, FR-75231 Paris Cedex 05, France
[9]CERN, CH-1211 Geneva 23, Switzerland
[10]Institut de Recherches Subatomiques, IN2P3 - CNRS/ULP - BP20, FR-67037 Strasbourg Cedex, France
[11]Now at DESY-Zeuthen, Platanenallee 6, D-15735 Zeuthen, Germany
[12]Institute of Nuclear Physics, N.C.S.R. Demokritos, P.O. Box 60228, GR-15310 Athens, Greece
[13]FZU, Inst. of Phys. of the C.A.S. High Energy Physics Division, Na Slovance 2, CZ-182 21, Praha 8, Czech Republic
[14]Dipartimento di Fisica, Università di Genova and INFN, Via Dodecaneso 33, IT-16146 Genova, Italy
[15]Institut des Sciences Nucléaires, IN2P3-CNRS, Université de Grenoble 1, FR-38026 Grenoble Cedex, France
[16]Helsinki Institute of Physics and Department of Physical Sciences, P.O. Box 64, FIN-00014 University of Helsinki, Finland
[17]Joint Institute for Nuclear Research, Dubna, Head Post Office, P.O. Box 79, RU-101 000 Moscow, Russian Federation
[18]Institut für Experimentelle Kernphysik, Universität Karlsruhe, Postfach 6980, DE-76128 Karlsruhe, Germany
[19]Institute of Nuclear Physics PAN,Ul. Radzikowskiego 152, PL-31142 Krakow, Poland
[20]Faculty of Physics and Nuclear Techniques, University of Mining and Metallurgy, PL-30055 Krakow, Poland
[21]Université de Paris-Sud, Lab. de l'Accélérateur Linéaire, IN2P3-CNRS, Bât. 200, FR-91405 Orsay Cedex, France
[22]School of Physics and Chemistry, University of Lancaster, Lancaster LA1 4YB, UK
[23]LIP, IST, FCUL - Av. Elias Garcia, 14-1^{o}, PT-1000 Lisboa Codex, Portugal
[24]Department of Physics, University of Liverpool, P.O. Box 147, Liverpool L69 3BX, UK
[25]Dept. of Physics and Astronomy, Kelvin Building, University of Glasgow, Glasgow G12 8QQ
[26]LPNHE, IN2P3-CNRS, Univ. Paris VI et VII, Tour 33 (RdC), 4 place Jussieu, FR-75252 Paris Cedex 05, France
[27]Department of Physics, University of Lund, Sölvegatan 14, SE-223 63 Lund, Sweden
[28]Université Claude Bernard de Lyon, IPNL, IN2P3-CNRS, FR-69622 Villeurbanne Cedex, France
[29]Dipartimento di Fisica, Università di Milano and INFN-MILANO, Via Celoria 16, IT-20133 Milan, Italy
[30]Dipartimento di Fisica, Univ. di Milano-Bicocca and INFN-MILANO, Piazza della Scienza 3, IT-20126 Milan, Italy
[31]IPNP of MFF, Charles Univ., Areal MFF, V Holesovickach 2, CZ-180 00, Praha 8, Czech Republic
[32]NIKHEF, Postbus 41882, NL-1009 DB Amsterdam, The Netherlands
[33]National Technical University, Physics Department, Zografou Campus, GR-15773 Athens, Greece
[34]Physics Department, University of Oslo, Blindern, NO-0316 Oslo, Norway
[35]Dpto. Fisica, Univ. Oviedo, Avda. Calvo Sotelo s/n, ES-33007 Oviedo, Spain
[36]Department of Physics, University of Oxford, Keble Road, Oxford OX1 3RH, UK
[37]Dipartimento di Fisica, Università di Padova and INFN, Via Marzolo 8, IT-35131 Padua, Italy
[38]Rutherford Appleton Laboratory, Chilton, Didcot OX11 OQX, UK
[39]Dipartimento di Fisica, Università di Roma II and INFN, Tor Vergata, IT-00173 Rome, Italy
[40]Dipartimento di Fisica, Università di Roma III and INFN, Via della Vasca Navale 84, IT-00146 Rome, Italy
[41]DAPNIA/Service de Physique des Particules, CEA-Saclay, FR-91191 Gif-sur-Yvette Cedex, France
[42]Instituto de Fisica de Cantabria (CSIC-UC), Avda. los Castros s/n, ES-39006 Santander, Spain
[43]Inst. for High Energy Physics, Serpukov P.O. Box 35, Protvino, (Moscow Region), Russian Federation
[44]J. Stefan Institute, Jamova 39, SI-1000 Ljubljana, Slovenia
[45]Laboratory for Astroparticle Physics, University of Nova Gorica, Kostanjeviska 16a, SI-5000 Nova Gorica, Slovenia
[46]Department of Physics, University of Ljubljana, SI-1000 Ljubljana, Slovenia
[47]Fysikum, Stockholm University, Box 6730, SE-113 85 Stockholm, Sweden
[48]Dipartimento di Fisica Sperimentale, Università di Torino and INFN, Via P. Giuria 1, IT-10125 Turin, Italy
[49]INFN,Sezione di Torino and Dipartimento di Fisica Teorica, Università di Torino, Via Giuria 1, IT-10125 Turin, Italy
[50]Dipartimento di Fisica, Università di Trieste and INFN, Via A. Valerio 2, IT-34127 Trieste, Italy
[51]Istituto di Fisica, Università di Udine and INFN, IT-33100 Udine, Italy
[52]Univ. Federal do Rio de Janeiro, C.P. 68528 Cidade Univ., Ilha do Fundão BR-21945-970 Rio de Janeiro, Brazil
[53]Department of Radiation Sciences, University of Uppsala, P.O. Box 535, SE-751 21 Uppsala, Sweden
[54]IFIC, Valencia-CSIC, and D.F.A.M.N., U. de Valencia, Avda. Dr. Moliner 50, ES-46100 Burjassot (Valencia), Spain
[55]Institut für Hochenergiephysik, Österr. Akad. d. Wissensch., Nikolsdorfergasse 18, AT-1050 Vienna, Austria
[56]Inst. Nuclear Studies and University of Warsaw, Ul. Hoza 69, PL-00681 Warsaw, Poland
[57]Now at University of Warwick, Coventry CV4 7AL, UK
[58]Fachbereich Physik, University of Wuppertal, Postfach 100 127, DE-42097 Wuppertal, Germany
† deceased

1 Introduction

The study of four-fermion processes in e^+e^- interactions becomes increasingly important as the centre-of-mass energy and the corresponding luminosity increase. The main goal of such studies is to verify the Standard Model predictions and to look for, or to set limits on, possible contributions arising from mechanisms beyond the Standard Model: for instance, anomalous triple gauge couplings [1] can usually give contributions to four-fermion final states. Moreover, such processes form an important background to new particle searches, such as those for charginos, neutralinos or non-standard Higgs bosons, and deviations from the Standard Model expectations would be a signal of new physics. LEP has provided a unique opportunity to study four-fermion interactions at several energies. On-shell pair production of W [2] and Z [3,4] bosons has been studied extensively. The focus of this paper is the measurement of the cross-section of neutral current processes with a Z and an off-shell photon ($Z\gamma^*$ in the following). To this end, several channels were studied: $l^+l^-q\bar{q}$ ($l \equiv e, \mu$), $q\bar{q}\nu\bar{\nu}$, $l^+l^-l'^+l'^-$ ($l, l' \equiv e, \mu, \tau$) and $q\bar{q}q\bar{q}$ (with a low mass $q\bar{q}$ pair). In addition, for $l^+l^-l'^+l'^-$ final states, a measurement of the total neutral current cross-section has been performed.

Figure 1 shows the main Feynman diagrams for four-fermion neutral current production in e^+e^- collisions. When there are no electrons in the final state these processes are dominated by the conversion processes shown in figure 1a. This graph represents eight different diagrams, usually referred to as the NC08 diagrams: two of them (usually referred to as NC02) lead to ZZ production, two to $\gamma^*\gamma^*$ and four to $Z\gamma^*$. These four $Z\gamma^*$ conversion diagrams are sketched in figure 2, and the square of their summed amplitudes is used in the definition of the signal to be measured in this paper, as explained below. A prominent feature of the graphs in figure 2 is the very different scale of the momentum transfer at the $Zf\bar{f}$ and $\gamma f\bar{f}$ vertices, an issue which must be properly addressed by the simulation programs (see section 3). For final states with electrons, other processes, such as t-channel γ exchange accompanied by Z^*/γ^*-strahlung (figure 1c) and multiperipheral production (figure 1d), contribute significantly. In particular, the processes originating from the bremsstrahlung diagram (1c), usually referred to as Zee and γ^*ee, represent an important background to the measurements with electrons presented in this paper (see sections 4 and 6). Interference effects of these processes with those originating from $Z\gamma^*$ can also be important and have to be taken into account.

The $Z\gamma^*$ production cross-section depends weakly on the centre-of-mass energy, but strongly on the mass of the virtual photon. For real photon production, $e^+e^- \to Z\gamma$, the cross-section reaches values above 100 pb, while in the kinematic region of $Z\gamma^*$ production considered in this paper, its value is generally in the region of a fraction of a picobarn. Furthermore, in the $Z\gamma^*$ production processes, particles coming from the conversion of low mass γ^*s into hadrons or leptons are preferentially produced at very small angles with respect to the beam direction. A measurement of this cross-section has thus to be performed for a specific selection of the γ^* mass and production polar angle.

Data collected by the DELPHI experiment in 1997-2000 at centre-of-mass energies from 183 to 209 GeV were used, corresponding to an integrated luminosity of about 667 pb^{-1}. Results for each channel are given in the form of a comparison of the predicted numbers of selected events with those found in data. Combination of channel results into an overall $Z\gamma^*$ cross-section is then performed. The resulting measurement is compared to the Standard Model expectation. The results presented here complement and augment those reported in previous studies of neutral current four-fermion production at LEP [5].

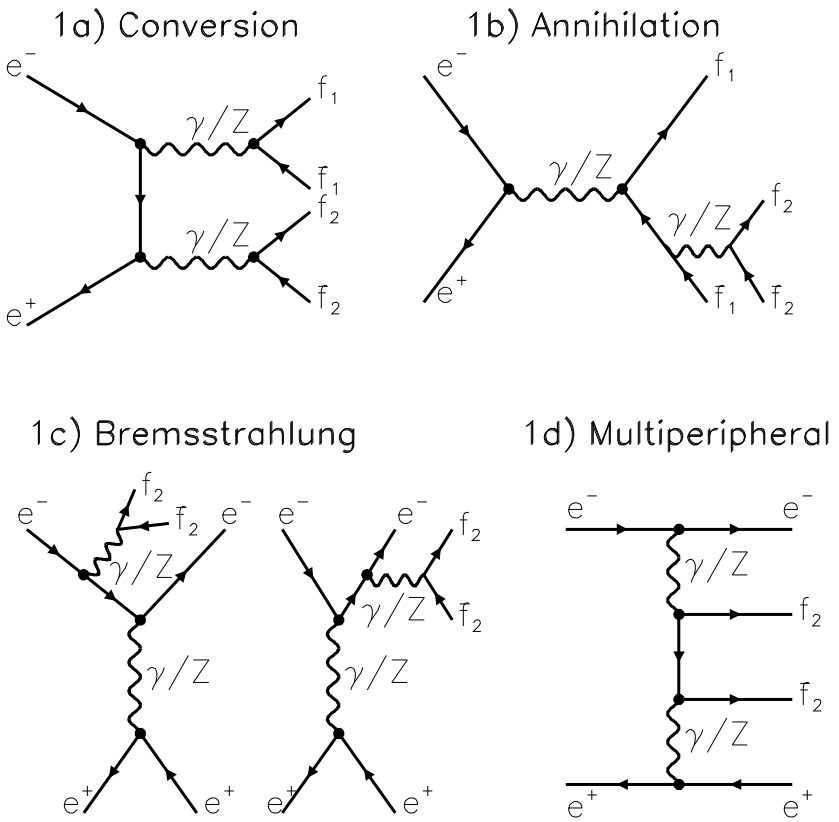

Figure 1: The Feynman diagrams for four-fermion neutral current production in e^+e^- collisions.

This paper is organised as follows. Two definitions of the $Z\gamma^*$ signal are given in section 2, one, the "Matrix Element definition", according to the Feynman diagrams contributing to $Z\gamma^*$ production, the other, the "LEP definition", using invariant mass cuts. Short descriptions of the detector, of the available data sets and of the simulation programs used in the analyses are given in section 3. The subsequent sections provide descriptions of the analyses used for the first signal definition for each of the channels studied: $l^+l^-q\bar{q}$ (section 4), $q\bar{q}\nu\bar{\nu}$ (section 5), $l^+l^-l'^+l'^-$ (section 6, where a total cross-section measurement is also presented), and $q\bar{q}q\bar{q}$ (section 7). The results using the Matrix Element signal definition are presented in section 8, while the analyses and results using the LEP signal definition are described in section 9. Conclusions are given in section 10.

2 Signal definition

Two different signal definitions were adopted in the analyses presented in this paper:

- **The Matrix Element definition:** For each of the final states considered, the signal was first defined by applying the following kinematic selection on all charged fermions at generator level:
$$|\cos\theta_{f^\pm}| < 0.98 \ ,$$
where $\theta_{f^\pm}$ is the polar angle of the charged fermion with respect to the beam axis. Events with one or more charged fermions not fulfilling these selections were considered as background. Then, for the surviving events, the signal was defined as the $Z\gamma^*$ contribution coming from the four conversion diagrams shown in figure 2. This was achieved by weighting the events in the selected generator-level sample by the quantity
$$\frac{|\mathcal{M}_{Z\gamma^*}|^2}{|\mathcal{M}_{all}|^2} \ ,$$
where $\mathcal{M}_{Z\gamma^*}$ and $\mathcal{M}_{all}$ are the matrix elements for $Z\gamma^*$ and for all the graphs in figure 1, respectively. Analogously, using the same weighting technique, the components obtained by weighting events by the quantities $\frac{|\mathcal{M}_{all-Z\gamma^*}|^2}{|\mathcal{M}_{all}|^2}$ and $1 - \frac{|\mathcal{M}_{Z\gamma^*}|^2}{|\mathcal{M}_{all}|^2} - \frac{|\mathcal{M}_{all-Z\gamma^*}|^2}{|\mathcal{M}_{all}|^2}$ were considered as background: these components represent, respectively, the contributions arising from non-$Z\gamma^*$ four-fermion processes (including ZZ and $\gamma^*\gamma^*$, which are also produced via conversion diagrams) and from the interference effects between $Z\gamma^*$ and non-$Z\gamma^*$ graphs. Expected rates were thus computed using generated events weighted by the appropriate ratio. Efficiencies were defined from the simulated event samples as the ratio of selected weighted events over all weighted events.
- **The LEP definition:** The second definition was agreed between the LEP Collaborations in order to combine results in a meaningful way. It is based on invariant mass cuts at generator level and explicitly avoids the difficult regions of low di-fermion masses. Depending on the final state, the following cuts were applied on invariant masses of fermion pairs and, where relevant, on lepton production polar angles: $M_{q\bar{q}} > 10$ GeV/c^2, $M_{l^+l^-} > 5$ GeV/c^2, $|\cos\theta_{l^\pm}| < 0.95$. Furthermore, it was required that only one fermion pair in the event had an invariant mass, $M_{f^+f^-}$, satisfying $|M_{f^+f^-} - M_Z| < 2\Gamma_Z$, where M_Z and Γ_Z are the nominal mass and width of the Z boson. Only the three dominant channels in the final result combination ($\mu^+\mu^- q\bar{q}$, $e^+e^- q\bar{q}$ and $q\bar{q}\nu\bar{\nu}$) were analysed using the LEP signal definition.

In the rest of this paper, when not explicitly stated, it is implied that the Matrix Element signal definition is being used.

3 Detector description and simulation

A detailed description of the DELPHI detector and a review of its performance can be found in [6,7]. For LEP2 operations, the vertex detector was upgraded [8], and a set of scintillation counters was added to veto photons in blind regions of the electromagnetic calorimetry, at polar angles around $\theta = 40°$, $\theta = 90°$ and $\theta = 140°$.

The integrated luminosity of 666.7 pb^{-1} collected by the DELPHI detector at centre-of-mass energies from 182.7 to 209 GeV was used in the analysis. The luminosities collected at various centre-of-mass energies are shown in table 1.

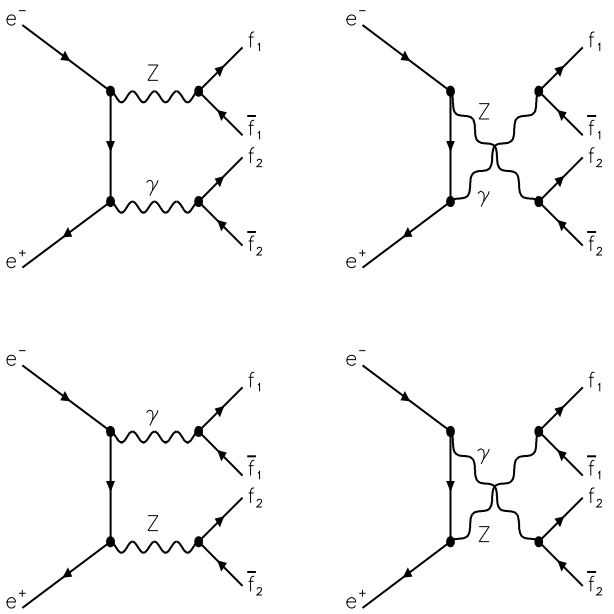

Figure 2: Neutral current conversion diagrams for the $Z\gamma^*$ process.

During the year 2000, one sector (1/12) of the main tracking device, the Time Projection Chamber (TPC), was inactive from the beginning of September to the end of data taking, which corresponded to about a quarter of the 2000 data sample. The effect was taken into account in the detector simulation and the corresponding small change of analysis sensitivity for this period was considered in the extraction of the cross-sections.

Simulated events were produced with the DELPHI simulation program DELSIM [7] and then passed through the same reconstruction chain as the data. The generation of processes leading to four-fermion final states, mediated by charged and neutral currents, was done with WPHACT [9,10], interfaced to the PYTHIA [11] fragmentation and hadronisation model. For the charged current part, WPHACT incorporates the $O(\alpha)$ Double Pole Approximation [12,13] radiative corrections to the doubly resonant WW production diagrams via a weighting technique, with the matrix elements provided by the YFSWW generator [14]. At a general level, WPHACT performs fully massive calculations all over the phase space, includes higher-order corrections and uses the package QEDPS [15] for initial state radiation. Two additional features, particularly relevant for the analyses described in this paper, were implemented in WPHACT: the study of the most suitable scale to use for α_{QED} at the γ^* vertices of the diagrams in figure 2, and the treatment of the hadronisation of low mass virtual photons. The first of these problems was solved in WPHACT by implementing the running of α_{QED} at the level of the event generation, thus using the value of the coupling constant corresponding to the mass of the photon propagator at the γ^* vertices. The second problem was addressed by interfacing WPHACT with a special package [16] for the specific treatment of the hadronisation of low mass $q\bar{q}$ systems. This package provides a description of the hadronisation from the $\gamma^* \to q\bar{q}$ process in the mass region below 2 GeV/c^2 both due to the presence of hadronic resonances (with

Year	$\sqrt{s}$ [GeV]	Integrated luminosity [pb^{-1}]
1997	182.7	55.0
1998	188.6	158.1
1999	191.6	25.0
1999	195.5	77.0
1999	199.5	82.0
1999	201.6	41.0
2000	205.0	81.3
2000	206.5	147.3
Total	197.1	666.7

Table 1: Luminosity-weighted centre-of-mass energies and integrated luminosities of the data analysed. During the year 2000, the energies reached were in the range 202-209 GeV and clustered mainly around 205 and 206.5 GeV.

subsequent decays described by PYTHIA) and in the continuum, based on experimental e^+e^- data at low energy. This is particularly important for the $q\bar{q}\nu\bar{\nu}$ (section 5) and $q\bar{q}q\bar{q}$ (section 7) analyses, which explore the low mass $q\bar{q}$ region. Phase space cuts are applied in WPHACT and can be found in table 2 of [10]. The study of the backgrounds due to $q\bar{q}(\gamma)$, $\mu^+\mu^-(\gamma)$ and $\tau^+\tau^-(\gamma)$ production was made using the KK2f [17] model; $e^+e^-(\gamma)$ events were simulated with BHWIDE [18]. Two-photon interactions were generated using WPHACT for the regions in which the multiperipheral contribution is not dominant and using BDK [19] for the pure two-photon region; PYTHIA 6.143 was used to model two-photon processes with single and doubly resolved photons.

4 Study of the $l^+l^-q\bar{q}$ final state

In this section the analysis of the final state containing jets and a pair of identified muons or electrons is described. The two final state leptons in the process $e^+e^- \to l^+l^-q\bar{q}$ are usually well isolated from all other particles. This property can be used to select such events with high efficiency in both the muon and electron channels. Events with $\tau^+\tau^-$ pairs have not been considered here. This part of the analysis follows very closely the one performed in [3], where an identical final state was studied.

A loose hadronic preselection was first applied, requiring that the events have at least 7 charged particles and a charged energy above $0.30\sqrt{s}$. To suppress the radiative return to the Z (final state on-shell Z production with the emission of a hard initial state radiation (ISR) photon) the event was rejected if a photon with energy more than 60 GeV was found. The selection procedures were then carried out in a similar way for the $\mu^+\mu^-q\bar{q}$ and $e^+e^-q\bar{q}$ channels. In order to maximise the lepton identification efficiency, any charged particle with momentum exceeding 5 GeV/c was considered as a possible lepton candidate around which nearby photons, if present, could be clustered. This was found to be necessary to improve the energy evaluation in the presence of final state radiation from electrons. In the case of the $e^+e^-q\bar{q}$ channel, photons with energy between 20 GeV and 60 GeV were also considered as electron candidates in order to recover events in which the electron track was not reconstructed. For both electrons and muons, "strong" and "soft" identification criteria were then defined. Muons were considered as strongly

identified if selected by the standard DELPHI muon identification package [7], based mainly on finding associated hits in the muon chambers. For soft muon identification, only kinematic and calorimetric criteria were used. Electrons were considered as strongly identified when the energy deposited in the electromagnetic calorimeter exceeded 60% of the cluster energy or 15 GeV, whichever was greater, and when the energy deposited in the hadron calorimeter was less than a specified limit. For soft electron identification, only requirements on the momentum of the charged particle in the cluster and on the energy deposited in the hadron calorimeter were imposed. Electron candidates originating from applying the clustering procedure around a photon were considered as softly identified. Events with at least two lepton candidates of the same flavour and opposite charge were then selected.[1] All particles except the lepton candidates were clustered into two jets and a kinematic fit requiring four-momentum conservation was applied, after appropriately adjusting the errors on lepton energies in cases where photons had been added by the clustering procedure.

At least one of the two lepton candidates was required to satisfy strong lepton identification criteria, while softer requirements were specified for the second.

Two discriminating variables were then used for final event selection: P_t^{min}, the lesser of the transverse momenta of the lepton candidates with respect to the nearest jet, and the χ^2 per degree of freedom of the kinematic fit. Cuts on these variables were applied, with values depending on the final state and on the quality of the lepton identification (see [3]).

4.1 Results

The distribution of the reconstructed mass of one fermion pair when the mass of the second one is within 15 GeV/c^2 of the nominal Z mass is compared with the predictions of the Standard Model in figure 3, separately for $\mu^+\mu^- q\bar{q}$ and $e^+e^- q\bar{q}$ events. In the $\mu^+\mu^- q\bar{q}$ channel the $Z\gamma^*$ contribution is clearly separated from the background component and is mostly concentrated in the region of the decay $Z \to q\bar{q}$, as expected. In the $e^+e^- q\bar{q}$ case, the distribution is flatter, indicating the presence of non-resonant diagrams. In both channels there is good overall agreement between the observed and predicted numbers of events. In the $e^+e^- q\bar{q}$ channel an accumulation of events is observed in the invariant mass distribution of the e^+e^- pair in the region between 50 and 60 GeV/c^2, with 7 events observed where 2.4 are expected. Various studies and comparisons with results of the other LEP experiments were performed, leading to the conclusion that this excess is most probably due to a statistical fluctuation.

The bidimensional distributions in the plane of the masses of the two fermion pairs predicted by the Standard Model are shown in figure 4 for the two channels studied, separately for $Z\gamma^*$ and background. The presence of non-resonant contributions, particularly of the type Zee and γ^*ee, is clearly visible in the $e^+e^- q\bar{q}$ case. The distributions were binned as shown graphically in figure 4, using a small number of irregularly sized bins. This allowed the regions where most of the background is concentrated to be avoided, except for the Zee contribution, while keeping as much signal as possible. Bin sizes were chosen in order to have an approximately equiprobable distribution of simulated events, with a finer binning in $e^+e^- q\bar{q}$ so as to follow better the more complicated structure of the background distribution. The observed and predicted numbers of events selected by this procedure at each energy point are reported in table 2.

[1] The requirement of having leptons of opposite charge was dropped in the case of candidate electrons originally identified as photons, for which no charge information is available.

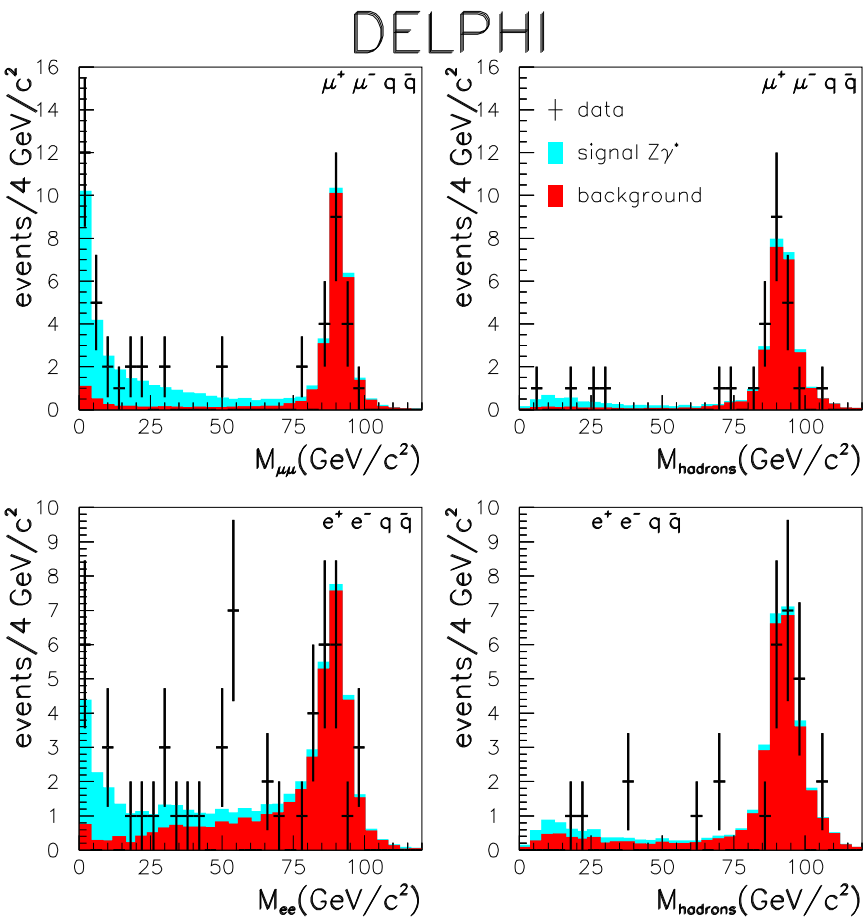

Figure 3: $l^+l^-q\bar{q}$ final state: Distributions of the mass of one fermion pair when the mass of the second is within 15 GeV/c^2 of M_Z. The two lower plots are for the $e^+e^-q\bar{q}$ channel and the two upper plots for the $\mu^+\mu^-q\bar{q}$ channel. The points are the data summed over all energy points, the dark (red) histogram is the distribution of the background predicted by the Standard Model, and the light (light blue) histogram is the predicted distribution of the $Z\gamma^*$ signal.

On combining the data from all energy points, the efficiency and purity of the selected $\mu^+\mu^-q\bar{q}$ sample were estimated from the simulation to be 42.0% and 84.7%, respectively. The background is composed of $\mu^+\mu^-q\bar{q}$ events outside the signal definition and of contributions from other final states. Interference effects in the $\mu^+\mu^-q\bar{q}$ channel in the region considered are negligible, as they account for less than 0.1% of the $Z\gamma^*$ cross-section. The predicted composition of the background is shown in table 3.

In the $e^+e^-q\bar{q}$ channel, the purity of the selected sample is estimated to be only 49.2%, mostly because of the unavoidable Zee background, while the efficiency was evaluated to be 24.3%. Interference effects between $Z\gamma^*$ and other four-fermion processes were estimated to account for -15% and are thus not negligible: they are mostly concentrated in the region of $Z\gamma^*$ - Zee overlap. The predicted composition of the background is shown in table 3.

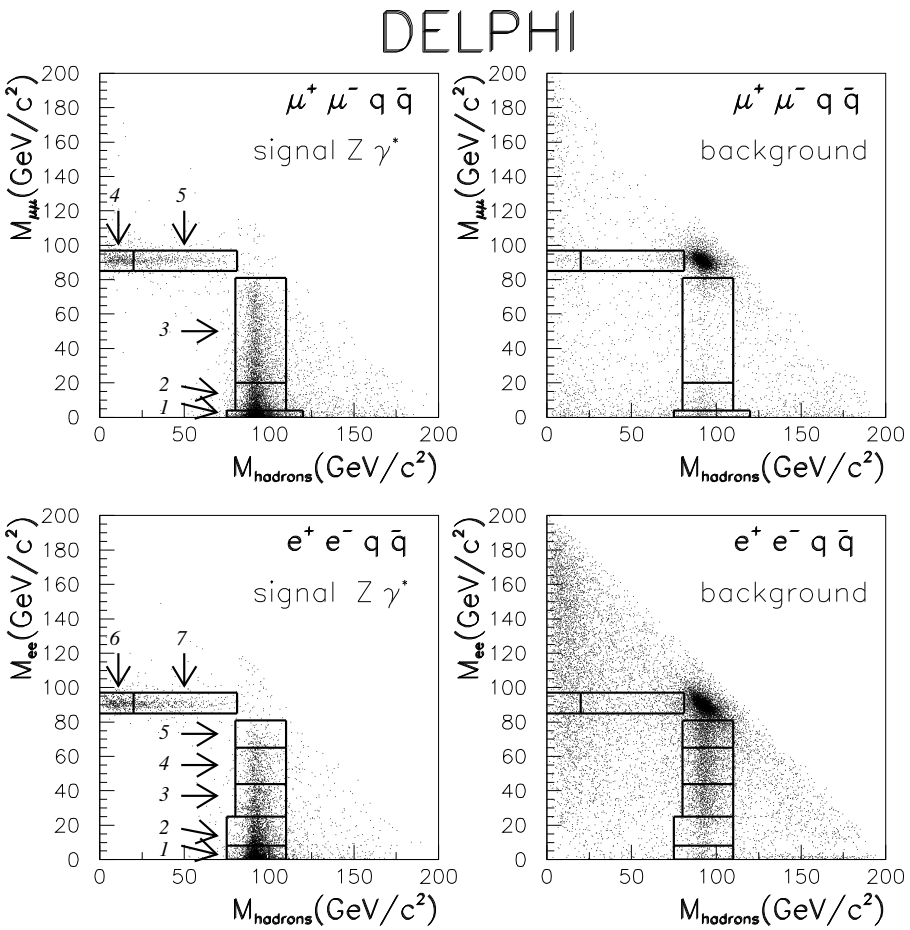

Figure 4: $l^+l^-q\bar{q}$ final state: Bidimensional distributions in the plane of the di-fermion masses predicted by the Standard Model for signal $Z\gamma^*$ (left-hand plots) and background (right-hand plots) for the two channels studied, averaged over all energy points. The bins used for the fit are also shown.

In order to disentangle the $Z\gamma^*$ from the Zee contribution more effectively, the distribution of the polar angle of the direction of the e^+e^- pair was studied as a function of the reconstructed invariant mass M_{ee} in the range defined by the first five bins in figure 4. Correlation plots are shown in figure 5 for signal and background: the distributions are well separated because in the Zee case, which dominates the background, even e^+e^- pairs of large invariant mass are emitted at low polar angles, due to the t-channel nature of the production process. The binning in figure 4 was therefore modified, as shown in figure 5, by doubling each bin, depending on whether a) the polar angle of the direction of the e^+e^- pair was in the barrel region ($40^\circ < \theta_{ee} < 140^\circ$) or in the endcap region ($\theta_{ee} < 40^\circ$ or $\theta_{ee} > 140^\circ$) for bins 1-5, and b) the polar angle of the direction of the hadronic system was in the barrel or in the endcap region for bins 6-7. A total of 14 bins was thus used for the $e^+e^-q\bar{q}$ cross-section measurement. This procedure resulted in an 8% reduction of the statistical error compared to the case where only mass bins were used.

The value of the $Z\gamma^*$ cross-section at each energy point was extracted using a binned likelihood fit technique (see section 8) and the values were then combined to get global

E (GeV)	$\mu^+\mu^- q\bar{q}$				$e^+e^- q\bar{q}$			
	Data	Total MC	Signal	Background	Data	Total MC	Signal	Background
182.7	8	3.4	2.9	0.5	4	3.3	1.8	1.5
188.6	8	9.3	7.8	1.5	10	9.7	4.6	5.1
191.6	0	2.1	1.9	0.2	1	1.4	0.7	0.7
195.5	2	4.1	3.5	0.6	7	4.1	2.1	2.0
199.5	4	4.4	3.7	0.7	5	4.1	2.0	2.1
201.6	3	2.1	1.8	0.3	6	2.1	1.0	1.1
205.0	4	3.9	3.3	0.6	1	4.1	2.0	2.1
206.5	6	7.4	6.2	1.2	5	7.4	3.6	3.8
Total	35	36.7	31.1	5.6	39	36.2	17.8	18.4

Table 2: Observed numbers of events in the $\mu^+\mu^- q\bar{q}$ and $e^+e^- q\bar{q}$ channels at each energy compared with the Standard Model predictions for signal and background.

Background source	$\mu^+\mu^- q\bar{q}$	$e^+e^- q\bar{q}$
WW	0.8	1.6
$q\bar{q}(\gamma)$	0.1	1.8
$\tau^+\tau^- q\bar{q}$	2.5	2.6
non-$Z\gamma^*$ $l^+l^- q\bar{q}$	2.2	18.0
Interference	< 0.001	-5.6
Total	5.6	18.4

Table 3: Composition of the background to $Z\gamma^*$ production in the $\mu^+\mu^- q\bar{q}$ and $e^+e^- q\bar{q}$ final states predicted by the Standard Model. The entries show the expected numbers of events, summed over all energy points. The row labelled non-$Z\gamma^*$ $l^+l^- q\bar{q}$ shows the four-fermion neutral current contributions from processes leading to the same final state as the signal, but defined as background, as described in section 1.

results, separately for $\mu^+\mu^- q\bar{q}$ and $e^+e^- q\bar{q}$. Only the value of the $Z\gamma^*$ contribution was varied in the fit, while all non-$Z\gamma^*$ contributions, backgrounds and interference terms were fixed to the Standard Model expectations. Figure 6 compares the data in each bin used in the fits to the $\mu^+\mu^- q\bar{q}$ and $e^+e^- q\bar{q}$ final states with the results of the fit, showing the contributions from the $Z\gamma^*$ signal, from the non-$Z\gamma^*$ component of each of the final states, from the interference terms, and from the other sources of background.

These results were used to derive the combined values of the $Z\gamma^*$ cross-section for the Matrix Element signal definition, as described in section 8.

In the $e^+e^- q\bar{q}$ case, where the presence of non-resonant diagrams is relevant, a two-parameter fit was also performed as a consistency check, leaving both the $Z\gamma^*$ and the non-$Z\gamma^*$ contributions free to vary, while fixing the remaining background sources and interference terms to the Standard Model expectations. No significant change in the $Z\gamma^*$ cross-section result was observed, while the ratio $R^{e^+e^- q\bar{q}}_{non-Z\gamma^*}$ of the measured to the predicted cross-section of the non-$Z\gamma^*$ contribution to $e^+e^- q\bar{q}$ was determined to be $R^{e^+e^- q\bar{q}}_{non-Z\gamma^*} = 1.15\ ^{+0.26}_{-0.23}$, where the error is statistical only.

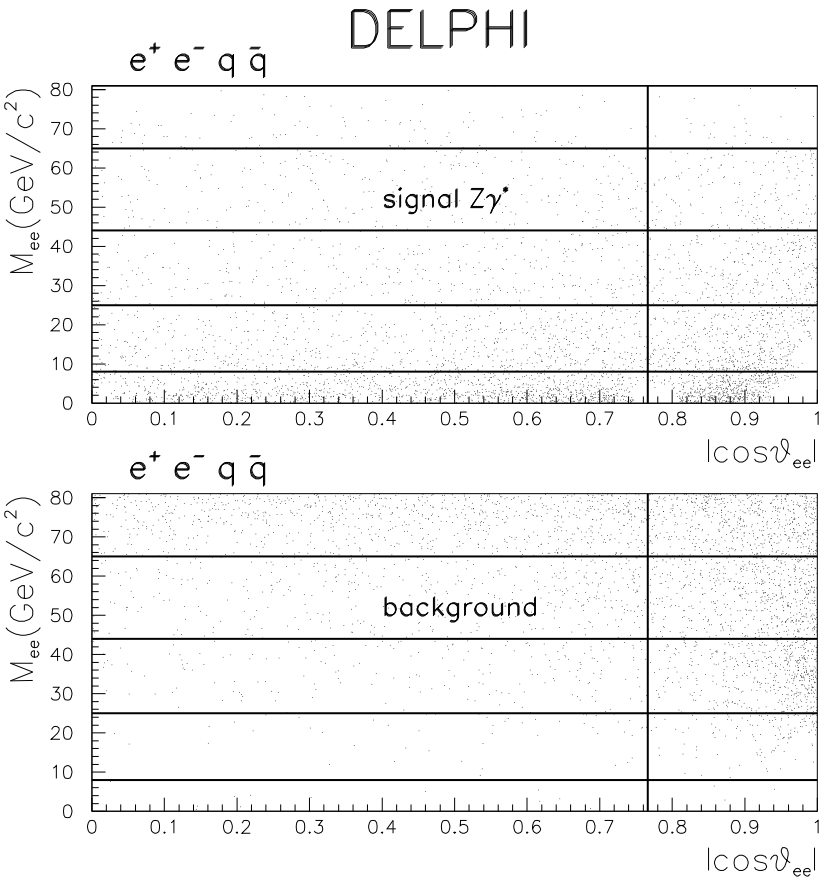

Figure 5: Distributions of the mass of the electron-positron pair in $e^+e^-q\bar{q}$ events for values of M_{ee} less than 80 GeV/c^2 versus the polar direction of the pair for signal $Z\gamma^*$ (upper plot) and background (lower plot) when the mass of the hadronic system is compatible with the Z mass. The plot shows the predictions of the Standard Model, averaged over all energy points. The binning adopted for these events follows that in figure 4 with an additional division into barrel and endcap regions, described in detail in the text.

4.2 Systematic errors

Several sources of systematic error were investigated.

Uncertainties in lepton identification, signal efficiency and background levels were evaluated using a procedure similar to that in [3], where the same final states were studied.

Uncertainties in the lepton identification were estimated by comparing semileptonic WW events selected in data and simulation using the strong lepton identification criteria. Uncertainties in signal efficiencies were evaluated by comparing the P_t^{min} and χ^2 distributions in data and simulation for all $llq\bar{q}$ events selected without mass cuts. Corresponding uncertainties in background levels were evaluated by comparing samples of events selected in data and in simulation, requiring both isolated tracks not to be identified as leptons, while maintaining all the other criteria. Finally, uncertainties in the background level in the $e^+e^-q\bar{q}$ channel from fake electrons were studied with $q\bar{q}(\gamma)$ events selected in data and in simulation with purely kinematic criteria. These effects and the statistical uncertainty of simulated data yielded a combined relative systematic error on the efficiency to

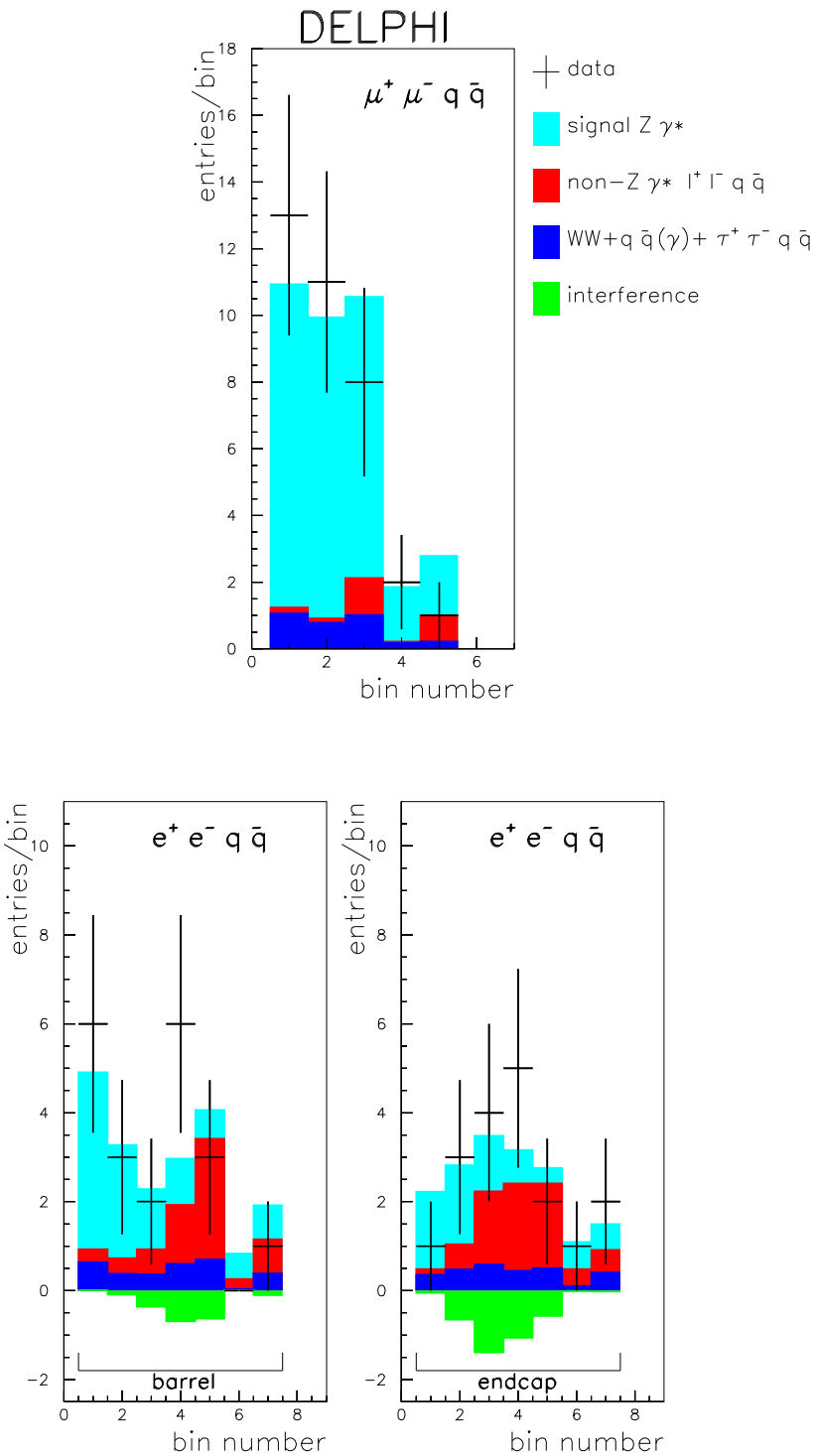

Figure 6: Results for $\mu^+\mu^- q\bar{q}$ (upper plot) and $e^+e^- q\bar{q}$ (lower plots). The points are data, summed over all energy points; the shaded histograms show the results of fits to the $Z\gamma^*$ component and the predicted Standard Model contributions from other sources. See figures 4 and 5 and the main text for the bin definitions.

select $\mu^+\mu^- q\bar{q}$ and $e^+e^- q\bar{q}$ events of $\pm 5.0\%$, and a relative uncertainty in the background level of $\pm 15\%$.[2]

Systematic effects coming from the fitting procedure were investigated. Fit results were found to be stable within the expected statistical uncertainties against variations of bin sizes, the number of bins and, for $e^+e^- q\bar{q}$, the number of fitted parameters. No systematic error was thus attributed to this source.

Possible systematic effects arising from the treatment in the fit of the $Z\gamma^*$ interference term with the other contributions (particularly the non-$Z\gamma^*$ one) were taken into account (see section 4.1) for $e^+e^- q\bar{q}$. Both the one-parameter and two-parameter fits were repeated and the interference term was weighted with a factor proportional to the product of the $Z\gamma^*$ and non-$Z\gamma^*$ amplitudes. This changed the cross-section result by 2%. Note, however, that this procedure neglects a possible change in the phase between the two interfering amplitudes with respect to that predicted in the Standard Model, and the procedure adopted therefore estimates the maximum possible effect that the unknown phase could have. A systematic uncertainty of $\pm 2\%$ was thus ascribed from this source for $e^+e^- q\bar{q}$ events.

The systematic error coming from the uncertainty in the luminosity measurement was evaluated to be $\pm 0.6\%$ both for $e^+e^- q\bar{q}$ and for $\mu^+\mu^- q\bar{q}$.

The total estimated systematic errors on the measured $Z\gamma^*$ cross-sections were $\pm 5\%$ for $\mu^+\mu^- q\bar{q}$ and $\pm 6\%$ for $e^+e^- q\bar{q}$.

5 Study of the $q\bar{q}\nu\bar{\nu}$ final state

The $q\bar{q}\nu\bar{\nu}$ channel is observed in a final state topology of hadronic matter and substantial missing energy. About half of the $Z\gamma^*$ cross-section in this channel comes from the region of $q\bar{q}$ masses below 6 GeV/c^2. Thus, final states often have the characteristic signature of "monojets", with the low invariant-mass hadronic system, which is the event visible mass, arising from the γ^* hadronisation and recoiling against a highly energetic $\nu\bar{\nu}$ pair which escapes detection.

Three analyses were performed and combined. The first analysis was intended to probe the low mass region of the hadronic system, so as to be efficient in the region of virtual photon mass, M_{γ^*}, below 6 GeV/c^2, where most of the cross-section is expected. It is denoted as the "low mass analysis" in the following. The second analysis exploited the large energy imbalance of $q\bar{q}\nu\bar{\nu}$ events, and retained some efficiency in the very low mass region of the hadronic system. It is denoted as the "energy asymmetry analysis" in the following. The third analysis was intended to have good overall efficiency for high M_{γ^*} at the expense of having very small efficiency in the low M_{γ^*} region. It is denoted as the "high mass analysis" in the following.

A common event preselection was defined for the three analyses, aimed mainly at reducing the backgrounds from two-photon and Bhabha events. The energy measured in the electromagnetic calorimeters was required to be less than 60 GeV in total and less than 10 GeV at polar angles below 15° and above 165°. Events with identified electrons at polar angles below 15° and above 165° were excluded; the visible energy of the event was required to exceed 15% of the centre-of-mass energy; the polar angle of the direction of the event missing momentum was required to be in the range $15° < \theta_{miss} < 165°$; and at least two charged particles with momentum greater than 200 MeV/c were required.

[2] In both cases determinations were limited in accuracy by the statistics of the available samples, and should be interpreted as upper bounds.

An extensive use of veto counters was implemented in all three analyses: events with hits in the photon veto counters far from energy deposits in calorimeters or reconstructed tracks were rejected. The details of the algorithms adopted are given in the following sections.

In order to increase the available statistics, no explicit lower cut on the reconstructed mass of the hadronic system was applied.

The numerical values of the cuts applied to kinematic variables in the three analyses were chosen using an optimisation procedure described in section 5.4 below.

5.1 Low mass analysis

Events with a visible mass $M_{vis} < 6$ GeV/c^2 and with visible energy E_{vis} larger than 20% of the centre-of-mass energy were selected. In addition, in order to limit the background from leptonic decays of Ws ($W \to e/\mu\ \nu$, $W \to \tau\nu$, $\tau \to e/\mu\ \nu$), it was required that no identified muon be present, while at most one electron was allowed in the event and its energy was required to be less than 30 GeV. Furthermore, events with the polar angle of the direction of the missing momentum in the range 38° to 42° (which is insufficiently covered by calorimeters, see section 3) were rejected. The event was then split into two hemispheres by the plane perpendicular to the thrust axis: events were rejected if there were hits in the photon veto counters in the hemisphere containing the direction of the missing momentum, while events with hits in the veto counters in the opposite hemisphere were accepted only if their angular separation from the closest charged-particle track or calorimetric energy deposit was less than 20°.

When used alone, this analysis selected 10 events in data and 6.7 in the simulation, of which 4.3 were signal and 2.4 were background.

5.2 Energy asymmetry analysis

In this analysis events were required to show a marked imbalance in the spatial distribution of the detected reaction products. Only events with total visible energy exceeding 20% of the centre-of-mass energy were accepted. Then two hemispheres were defined by a plane perpendicular to the direction of the thrust axis, and the total energy in each hemisphere was estimated from the curvature of charged-particle tracks and from calorimetric measurements. It was required that the energy in one of the two hemispheres account for at least 99% of the total energy in the event. This was the main topological selection of the analysis and provided an implicit upper cut-off on the total visible mass of events.

Signals from photon veto counters were used to discard events with possible loss of energetic photons in the insensitive regions of the electromagnetic calorimetry by adopting the same algorithm as in the low mass analysis (see section 5.1). In order to limit further the background from processes which have most of the cross-section in the forward region (mainly Bhabha and two-photon events), the cut on the polar angle of the direction of the missing momentum was tightened and required to lie in the range $25° < \theta < 155°$.

At this level, the background was completely dominated by the WW and $We\nu$ processes. In order to reject leptonic decays of Ws, events with identified muons were discarded, while events with at most one electron were kept if the energy of the electron did not exceed 25 GeV and the electron was not isolated, i.e. its angle with respect to the closest charged-particle track was not larger than 10°.

Additional selections were implemented in order to suppress further the WW and $We\nu$ backgrounds. Part of this background arises from hadronic decays of one W, accompanied by undetected leptons coming from the decay of the other W or lost in the beam pipe (especially in the case of $We\nu$). Such events usually show larger visible mass than is expected from signal events, due to the sizeable mass of the W boson. A selection on the event visible mass was thus imposed, requiring $M_{vis} < 45$ GeV/c^2. Another important fraction of the remaining background comes from WW events with both Ws decaying to τs, $W \to \tau\nu_\tau$, with the visible decay products boosted into the same hemisphere. The signature of these events is that a few particles carry most of the visible energy and have visible mass above a few GeV/c^2. Two more selections were imposed to reject such a source of background. Events with visible mass above 5 GeV/c^2 and with more than 90% of the visible energy carried by the two most energetic particles were discarded. The remaining events were forced into two jets with the LUCLUS algorithm [20]. Events with total particle multiplicity below 11 and an angle between the two jets above 30° were rejected.

When used alone, this analysis selected 25 events in data and 29.5 in the simulation, of which 17.3 were signal and 12.2 were background. Half of the background was contributed by the WW and $We\nu$ processes.

5.3 High mass analysis

In this analysis a cut on the multiplicity of charged-particle tracks was applied, requiring it to be larger than 4. This implied that the efficiency of the analysis dropped essentially to zero for $q\bar{q}$ masses below 2 GeV/c^2. The main topological selections were applied at jet level. Jets were reconstructed using the LUCLUS algorithm and the events were forced into a two-jet configuration. An upper cut on the opening angle of the two jets was set at 78°. The parameter d_2^{join} was defined to be the value for which the event passes from a two-jet to a single jet configuration: only events with $d_2^{join} < 30$ GeV/c were retained. The acoplanarity (defined as the complement of the angle between the jets projected on the plane perpendicular to the beams) was required to be larger than 90°. Then the event was split into two hemispheres about a plane perpendicular to the thrust axis and the energy asymmetry, evaluated as in section 5.2, was required to be larger than 95%. Events with missing mass less than 80 GeV/c^2 were rejected.

A further selection was imposed on the energy of the visible system, E_{vis}, rejecting events with $E_{vis} > 80$ GeV. In the absence of initial- and final-state radiation, the energy and the mass of the $q\bar{q}$ system in the $Z\gamma^*$ process are related in the following way:

$$E_{q\bar{q}} = \frac{s - M_Z^2 + M_{q\bar{q}}^2}{2\sqrt{s}} \ .$$

The quantity $E_{kin} = \frac{s - M_Z^2 + M_{vis}^2}{2\sqrt{s}}$ was defined, using the visible mass of the event. It was then required that the difference between E_{kin} and the visible energy of the event E_{vis} did not exceed 45 GeV. This cut, and the cut on E_{vis} described above, were effective in suppressing the WW and $q\bar{q}(\gamma)$ backgrounds.

Events with hits in the photon veto counters were accepted if the angular distance between these hits and the direction of the closest jet was less than 30°; otherwise they were rejected.

When used alone, this analysis selected 21 events in data and 20.7 in the simulation, of which 13.4 were signal and 7.3 were background. Most of the background is due to WW and $We\nu$ events.

5.4 Results

The three analyses were combined on an event-by-event basis, by selecting events which passed any of the three selections. Numerical values of the cuts were optimised in a two-stage procedure. First, for each analysis separately, all the cuts relevant to that analysis were varied such that the product of efficiency and purity of the selected sample was maximised. Then the most important cuts in each analysis were allowed to vary simultaneously, keeping the other cuts at the values obtained in the first stage, and the product of the efficiency and purity of the sample selected by any of the three analyses was maximised. (The values listed in sections 5.1, 5.2 and 5.3 are the result of this last optimisation procedure). In total, 42 events were found in data and 41.3 in the simulation (with a total overlap between the three selections of about 30%); of the simulated sample, 23.4 events were signal and 17.9 were background. The most abundant source of background was predicted to come from $We\nu$ events, which accounted for 7.9 events, mainly in the channel $q\bar{q}e\nu$ and partially in $\tau\nu e\nu$. On-shell WW processes contributed about 4 events to the background, with 2.9 of them containing at least one W decaying to $\tau\nu$. The remaining main sources of background were $q\bar{q}$ (about 2 events), $\tau\tau$ (about 2 events) and other four-fermion neutral current processes (1.1 events). Table 4 shows the numbers of signal and background events predicted by the Standard Model and the observed numbers of events in the $q\bar{q}\nu\bar{\nu}$ channel at the various centre-of-mass energies.

E (GeV)	Data	Total MC	Signal	Background
182.7	3	3.5	2.3	1.2
188.6	9	10.1	6.0	4.1
191.6	1	1.3	0.9	0.4
195.5	7	4.4	2.9	1.5
199.5	6	5.2	2.9	2.3
201.6	2	2.5	1.3	1.2
205.0	9	4.9	2.6	2.3
206.5	5	9.4	4.5	4.9
Total	42	41.3	23.4	17.9

Table 4: Observed numbers of events in the $q\bar{q}\nu\bar{\nu}$ channel at each energy compared with the Standard Model predictions for signal and background.

The differential efficiencies of the three analyses as a function of the generated mass, $M(q\bar{q})$, estimated from the simulation, are shown in figure 7, together with the efficiency for the combined selection. The overall selection efficiency, averaged over all masses, was estimated to be 38.8%. The distribution of the reconstructed visible mass, M_{vis}, for the 42 data events is shown in figure 8, which also shows the distributions for the simulated signal and background events. Good agreement is observed with the Standard Model expectations.

The value of the $Z\gamma^*$ cross-section at each energy point was extracted using a counting technique and the values were then combined to get a global result. All non-$Z\gamma^*$ contributions, backgrounds and interference terms were fixed to the Standard Model expectations. The result was used to derive a combined value for the $Z\gamma^*$ cross-section in the Matrix Element signal definition, as described in section 8.

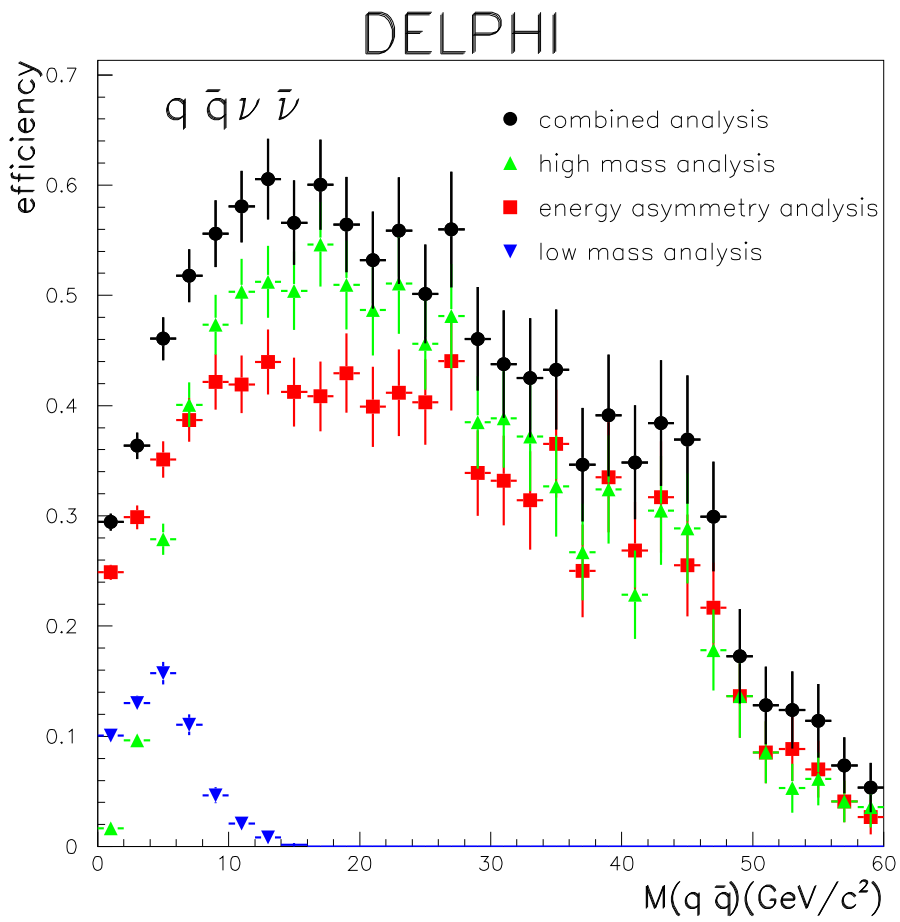

Figure 7: Selection efficiency of the $q\bar{q}\nu\bar{\nu}$ analyses, averaged over all energy points, as a function of the generated $M(q\bar{q})$ mass. The efficiency is shown for each of the three analyses (see text) separately, and for the combined analysis.

5.5 Systematic errors

Various sources of systematic error were considered.

The predicted background cross-sections were varied according to the following values: WW : $\pm 2\%$, $q\bar{q}$: $\pm 5\%$, $We\nu$: $\pm 5\%$, $\tau\tau$: $\pm 5\%$, four-fermion neutral current processes: $\pm 5\%$. The combined effect on the cross-section measurement was estimated to amount to $\pm 2\%$, with the main contribution coming from the uncertainty on the $We\nu$ cross-section.

Uncertainties on the signal efficiency coming from the Monte Carlo generator were studied by comparing different generator models. In particular, a sample of $q\bar{q}\nu\bar{\nu}$ was generated with the EXCALIBUR [21] four-fermion generator for masses of the hadronic system $M(q\bar{q}) > 10$ GeV/c^2. For generated masses below 10 GeV/c^2 the hadronisation model in EXCALIBUR is not as reliable as that in WPHACT and systematic effects from that region were evaluated separately (see below). The full analysis was applied to the EXCALIBUR sample and a difference of 3% in the signal efficiency was obtained. A systematic uncertainty of $\pm 3\%$ was thus conservatively ascribed to this source.

Systematic uncertainties due to the description of the hadronisation mechanism in the $q\bar{q}$ system were taken into account. It was assumed that these effects can be relevant

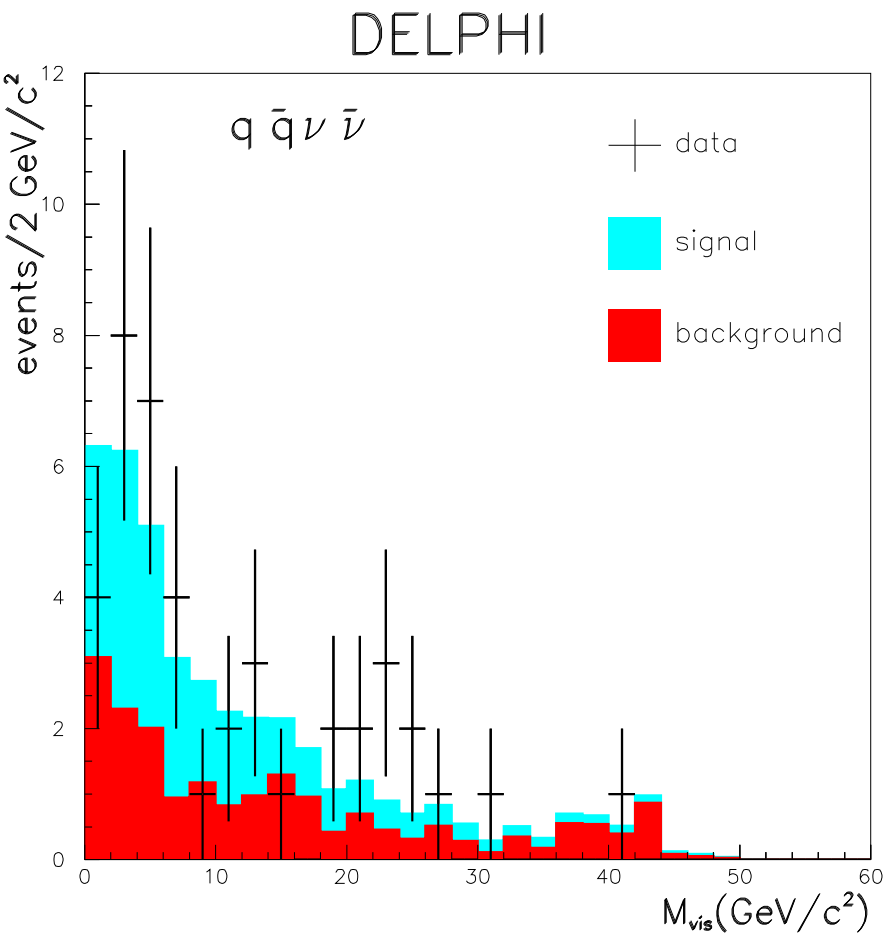

Figure 8: Distribution of the visible invariant mass of the hadronic system in the $q\bar{q}\nu\bar{\nu}$ selection, compared with the Standard Model predictions for signal and background. The points are the data, summed over all energy points, the light (light blue) histogram shows the predicted signal contribution, and the dark (red) histogram shows the predicted background.

for masses $M(q\bar{q}) < 10$ GeV/c^2 (see above), affecting the analysis mainly through corresponding uncertainties in charged-particle multiplicity distributions. These effects were not expected to be large because two of the three analyses (the low mass analysis and the energy asymmetry analysis) adopted a very low cut on the charged-particle multiplicity. The study of these effects was split into two parts, corresponding to the resonance and the continuum contributions respectively (see section 3). In the simulated sample the dominant resonances were identified, their corresponding detection efficiencies computed, and their contributions varied by amounts derived from the uncertainties in their known measured cross-sections: 1% for ρ and ϕ production, 10% for resonances decaying to final states with 3 or 4 charged particles, and 30% for resonances decaying to states with 5 or 6 charged particles. The effect on the estimated cross-section was found to be negligible; this is not surprising as ρ production, for which the cross-section is accurately determined, accounts for about 80% of the cross-section below 2 GeV/c^2. As a second step, the contribution of the resonances was subtracted from the hadronic mass distribution,

the charged-particle multiplicity distribution of the remaining sample studied and the analysis efficiency evaluated as a function of the number of charged particles. The effect of a possible error in the determination of the charged-particle multiplicity distribution was then estimated by stretching the observed distribution by +20%, rebinning, and applying the efficiency curve to the new distribution. The procedure was repeated, compressing the distribution by 20%. The range of cross-sections obtained from the stretched and compressed distributions was taken as an estimate of the systematic error. The effect on the $Z\gamma^*$ cross-section amounted to $\pm 4\%$.

Another source of systematic uncertainty considered was the reliability of the simulation in correctly estimating the amount of background. As explained in section 5.4, the main backgrounds are WW events, with one or both Ws decaying to τ, and $We\nu$ events, with the on-shell W decaying hadronically or to $\tau\nu$. These events share the common feature of having the decay products of one W detected on one side, and missing energy on the other side. The missing energy is due to the low angle electron, typically lost in the beam pipe in the $We\nu$ case, or to an undetected decay lepton or charged-particle track in the WW case. Furthermore, in both topologies, additional missing energy is carried by the escaping neutrino. In order to evaluate the reliability of the simulation in estimating the efficiency to detect backgrounds in such a topology, events with features similar to those of the background in the $q\bar{q}\nu\bar{\nu}$ analysis were studied. In particular, WW events with one W decaying to a detected lepton (electron or muon) or to an isolated charged-particle track, which was then artificially removed from the event, can mimic most of the WW and $We\nu$ background, with the second W playing the role of the hadronic signal. Therefore events with an isolated electron, muon or other charged-particle track were selected. Identified leptons or other charged-particle tracks were initially required to have momentum larger than 10 GeV/c and an angle with respect to the closest charged-particle track larger than 10°. The selected candidate track was then excluded from the event and the selections in sections 5.1, 5.2 and 5.3 applied to the remaining system. At the end of the procedure, 142 events with an isolated muon were found in data and 135.7 in the simulation, 110 events with an isolated electron were found in data and 115.1 in the simulation, and 79 events with a single isolated charged-particle track were found in data and 72.4 in the simulation. The distribution of the isolation angle of the selected lepton or single track after all the cuts is shown in figure 9. Good agreement between data and simulation is observed. The dominant contributions to the events selected in this way come from semileptonic WW production, $\tau\tau$ events and, to a lesser extent, Bhabha events, and can thus be used to emulate the background to the $q\bar{q}\nu\bar{\nu}$ signal: when the isolated lepton or other charged-particle track is excluded from the sample, the remaining system is strongly asymmetric in the angular distribution of the visible momentum, and of the same topology as the background expected in the $q\bar{q}\nu\bar{\nu}$ sample. (The estimated contribution from the $q\bar{q}\nu\bar{\nu}$ signal to this sample is totally negligible).

The agreement between data and simulation in figure 9 was subjected to more detailed checks, for example by selecting the region of the distribution in the isolation angle of the single charged-particle track which enriches the sample in WW events: two-fermion events preferentially populate the region of large isolation angle, being almost back to back, and their contribution can be greatly reduced with a cut at around 130°. Similarly, other checks were made for different visible-mass and track-multiplicity regions; in all the cases the agreement between data and simulation was good within the errors. The statistical error in the total of 331 events selected by this procedure was thus taken as an estimate of the systematic uncertainty due to the background evaluation from the simulation; this gave a contribution of $\pm 3\%$ on the $q\bar{q}\nu\bar{\nu}$ cross-section measurement.

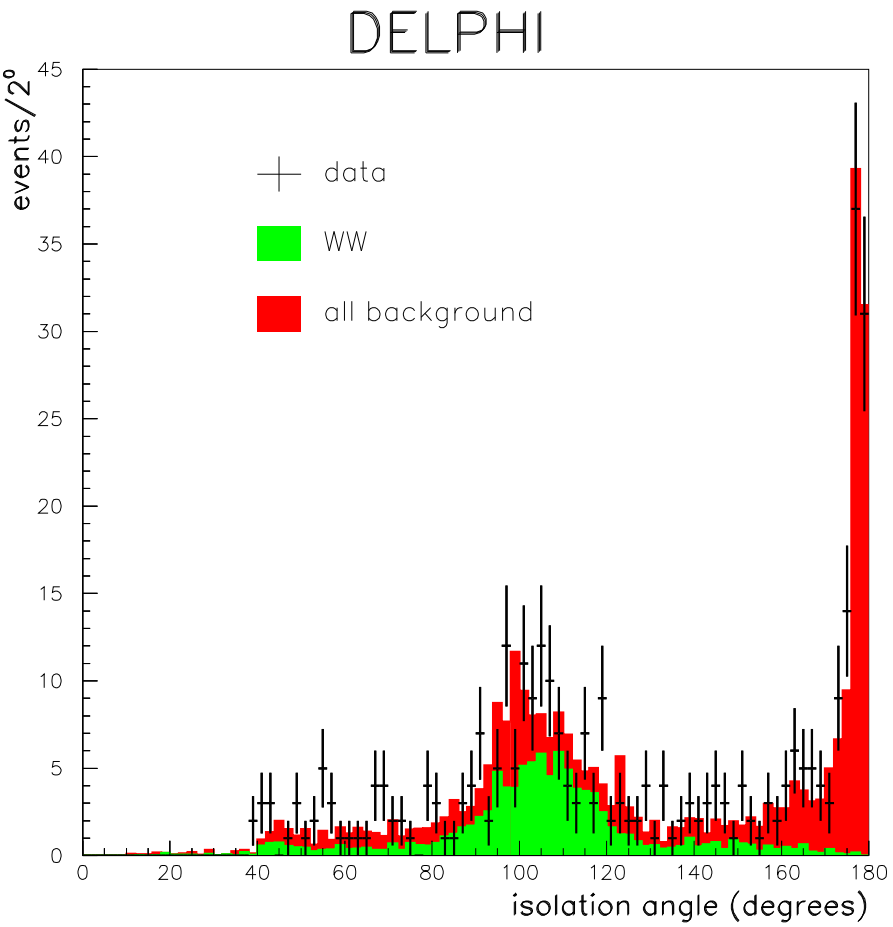

Figure 9: Isolation angle of selected electrons, muons and single charged-particle tracks in the sample selected to mimic the background to the selected $q\bar{q}\nu\bar{\nu}$ sample. The points are the data, summed over all energy points, the light (green) histogram is the predicted WW contribution, and the dark (red) histogram is the rest of the background.

Systematic uncertainties from the trigger efficiency were investigated and found to be negligible: the triggering efficiency for a single charged-particle track with transverse momentum $p_T > 3$ GeV/c is already very well determined [22], while in the present analyses a charged-particle track multiplicity of at least 2 was required, with transverse momenta of selected events in general well in excess of 3 GeV/c.

The systematic uncertainty coming from the luminosity measurement was estimated to give an error of $\pm 0.6\%$ on the cross-section measurement.

The statistical error from the limited simulated sample gave an uncertainty of $\pm 5\%$.

Finally, the stability of the result as a function of the applied experimental cuts was checked by varying the selections of the three analyses, first separately and then at the same time. The procedure set up to maximise the product of the efficiency and purity of the simulated sample (see section 5.4) was used to vary all the relevant cuts of sections 5.1, 5.2 and 5.3 within reasonable values; selections were accepted if the predicted value for the selected sample differed by less than the statistical error of the optimum value obtained from the simulated sample used in the analysis. For each such selection, the background

level and number of events in data were estimated and a value for the $q\bar{q}\nu\bar{\nu}$ cross-section was measured. The root mean square of the distribution of the cross-sections evaluated in this way was estimated to amount to 3%. As this number is compatible with the statistical fluctuations intrinsic to this procedure, no systematic error was added.

The total estimated systematic error on the $Z\gamma^*$ $q\bar{q}\nu\bar{\nu}$ cross-section measurement was thus estimated to be $\pm 8\%$.

6 Study of the $l^+l^-l'^+l'^-$ final state

The Feynman diagrams of figure 1 give rise to six possible final states with four charged leptons: $\mu^+\mu^-\mu^+\mu^-$, $e^+e^-e^+e^-$, $\tau^+\tau^-\tau^+\tau^-$, $e^+e^-\mu^+\mu^-$, $e^+e^-\tau^+\tau^-$ and $\mu^+\mu^-\tau^+\tau^-$. These final states have a rather clean experimental signature, but do not contribute significantly to the total four-fermion production cross-section due to the low branching fraction of $Z/\gamma^* \to l^+l^-$.

The selection of events in the $l^+l^-l'^+l'^-$ final state was restricted to topologies with four well reconstructed charged particles with momenta larger than 2 GeV/c (henceforth called lepton candidates). Events with two additional well-measured charged particles with opposite charges were allowed, provided that the pair was compatible with a photon conversion, or that the momentum of both particles was less than 2 GeV/c. Five additional charged particles were allowed in the event if their tracks did not point to the vertex; such tracks were not considered in the following steps of the analysis. The previous selections implied that for $e^+e^-\tau^+\tau^-$, $\mu^+\mu^-\tau^+\tau^-$and $\tau^+\tau^-\tau^+\tau^-$ events only one-prong τ decays were considered. The sum of the charges of the lepton candidates had to equal zero and the angle between the directions of any two of them had to be larger than 5°.

The four lepton candidates were required to fulfil the following additional selection criteria: the momenta of at least three of them had to exceed 6 GeV/c, their total energy had to be greater than $0.25\sqrt{s}$ (to reject background from two-photon interactions), and the length of at least three of the candidates' tracks was required to be greater than 50 cm. Beam-gas and $\tau^+\tau^-\gamma$ events were rejected by requiring that the four lepton candidates were not all in the same hemisphere with respect to the beam direction. For data taken during 2000, in the period when one sector of the TPC was not working, a slightly more relaxed criterion for track selection was applied if the track traversed that sector.

Selected events in the data were compared with simulated signal and background samples generated at the eight centre-of-mass energies. The expected numbers of events for signal and background, together with the numbers of events found in data, are shown in table 5 both for the full sample of $l^+l^-l'^+l'^-$ events, selected as described above, and for the $Z\gamma^*$ sample defined in section 6.2. The overall $l^+l^-l'^+l'^-$ selection efficiency is $\sim$15%, increasing slightly with $\sqrt{s}$ for the full sample, while for the $Z\gamma^*$ selection it ranges between 22% and 30%. The most important contribution to the non-$l^+l^-l'^+l'^-$ background comes from $e^+e^- \to e^+e^-q\bar{q}$ events with low $q\bar{q}$ mass. The second most important contribution is due to the $e^+e^- \to \tau^+\tau^-(\gamma)$ process. Good agreement was found between the data and the predictions of the simulation after each selection was applied sequentially. For the $Z\gamma^*$ sample, the main background is due to $l^+l^-l'^+l'^-$ contributions from non-$Z\gamma^*$ processes.

E (GeV)	$l^+l^-l'^+l'^-$ full sample				$l^+l^-l'^+l'^-$ $Z\gamma^*$ sample			
	Data	Total MC	Signal	Background	Data	Total MC	Signal	Background
182.7	3	3.9	3.4	0.4	1	1.5	0.5	1.0
188.6	14	12.4	10.0	2.4	2	4.8	1.6	3.2
191.6	1	1.8	1.6	0.2	1	0.6	0.2	0.4
195.5	5	5.3	4.6	0.7	2	1.9	0.6	1.3
199.5	8	6.0	5.1	0.8	2	2.0	0.7	1.3
201.6	3	2.7	2.4	0.4	2	0.9	0.3	0.6
205.0	7	5.3	4.8	0.5	4	1.8	0.7	1.2
206.5	7	9.6	8.2	1.4	3	3.1	0.9	2.1
Total	48	47.0	40.1	6.8	17	16.6	5.5	11.1

Table 5: Observed numbers of events in the $l^+l^-l'^+l'^-$ channel for the full sample and for the $Z\gamma^*$ sample at each energy, compared with the Standard Model predictions for signal and background. In the case of the $Z\gamma^*$ sample, the background contributions are defined to include the non-$Z\gamma^*$ $l^+l^-l'^+l'^-$ contribution and the non-$l^+l^-l'^+l'^-$ contribution.

6.1 Particle identification and final state classification

Events selected in the $l^+l^-l'^+l'^-$ final state were classified into one of the six final states according to the number of identified muons, electrons and pions. A constrained fit procedure was also used to complete the identification.

Muon identification was performed by combining the standard DELPHI identification package [7] in the muon chambers with the energy deposition profile in the hadron calorimeter and the energy deposited in the electromagnetic calorimeter.

Electron identification required that there be no signal in the muon chambers and no energy deposited in the hadron calorimeter after the first layer. The energy in the electromagnetic calorimeter in a 2° cone surrounding the candidate particle was required to be larger than 1 GeV. For electrons satisfying these criteria, the momentum of the charged particle was replaced by the energy deposited in the electromagnetic calorimeter.

Pions were identified as tracks leaving an energy deposit in the electromagnetic calorimeter compatible with a minimum ionizing signal, no hits in the muon chambers and energy deposited in the layers of the hadron calorimeter compatible with the profile of a hadron shower.

The assignment of the final state proceeded as follows:

- If no e^+e^- or $\mu^+\mu^-$ pair was identified, the four particles were considered as τ decays and the final state to be $\tau^+\tau^-\tau^+\tau^-$;
- If two pairs were identified as e^+e^-, $\mu^+\mu^-$ or $\tau^+\tau^-$, the final state was considered to be fully identified;
- If one e^+e^- or $\mu^+\mu^-$ pair was identified and the second pair had two identified particles, different from one another, the event was considered to be $e^+e^-\tau^+\tau^-$ or $\mu^+\mu^-\tau^+\tau^-$, respectively. The second pair was also designated as $\tau^+\tau^-$ if only one particle was identified and was different from the identified pair, or if neither was identified;
- If the event had 3 identified electrons or muons and one unidentified particle, two hypotheses were considered: that the 4 particles were identical or that the unidentified particle was one of a $\tau^+\tau^-$ pair.

A constrained kinematic fit was then performed on the selected events, imposing four-momentum conservation. This implies a four-constraint fit in the case where both lepton pairs are either electrons or muons, and a two- or zero-constraint fit in the cases where, respectively, one or two tau pairs are assumed present, as the magnitude of the tau momentum was taken to be unknown. Where more than one kinematic hypothesis could be applied to the same event, the decision procedure and the final identification were based on the probability of the χ^2 of the fit and the relative errors of the fitted masses. In the case of four identical particles, the combination for which a pair of leptons had reconstructed mass within 15 GeV/c^2 of the nominal Z mass was chosen or, if this condition was not fulfilled, the combination with the largest fitted invariant mass of a pair of leptons was selected. If no acceptable hypothesis was found, further fits were tried where kinematically possible, assuming, in addition to the four leptons, the presence of an unobserved ISR photon in the beam pipe; again the best resulting fit was selected. Figure 10 shows the distributions of the larger and smaller mass pairs for the full data sample, calculated for each event from the results of the chosen fit, and compares them with the predictions of the Standard Model.

The efficiencies for assigning the correct final states to the selected events were estimated from the simulation. The results are summarised in table 6, which shows the expected numbers of events from the full $l^+l^-l'^+l'^-$ sample which were identified in each of the possible final states, as well as the efficiency and purity.

Identified final state	Generated final state								Data	Purity (%)
	$e^+e^-e^+e^-$	$e^+e^-\mu^+\mu^-$	$e^+e^-\tau^+\tau^-$	$\mu^+\mu^-\mu^+\mu^-$	$\mu^+\mu^-\tau^+\tau^-$	$\tau^+\tau^-\tau^+\tau^-$	Total	Bck		
$e^+e^-e^+e^-$	6.4	0.0	0.3	0.0	0.0	0.0	6.7	1.4	7	80
$e^+e^-\mu^+\mu^-$	0.0	13.8	0.3	0.0	0.1	0.0	14.2	0.4	14	95
$e^+e^-\tau^+\tau^-$	3.2	1.5	3.2	0.0	0.0	0.1	8.0	3.0	16	29
$\mu^+\mu^-\mu^+\mu^-$	0.0	0.0	0.0	2.3	0.1	0.0	2.4	0.1	2	92
$\mu^+\mu^-\tau^+\tau^-$	0.0	4.0	0.0	0.4	1.6	0.0	6.0	0.4	7	25
$\tau^+\tau^-\tau^+\tau^-$	0.4	0.5	0.6	0.0	0.2	0.2	1.9	1.5	2	6
Efficiency (%)	10	11	11	13	12	9				

Table 6: Upper six rows: Expected numbers of signal and background events and purity for each identified final state for the full $l^+l^-l'^+l'^-$ event sample, estimated from the simulation. The number of events found in the experimental data is also given for each final state. Bottom row: Estimated efficiency for selection and correct classification of each $l^+l^-l'^+l'^-$ state with respect to the total $l^+l^-l'^+l'^-$ content of the sample.

In 2% of the cases the events could not be classified in any of the six final states, as there was no complete *a priori* identification of all the particles in the event and the constrained fit failed. Due to lack of identification of electrons or muons, mainly in regions with poor coverage by the electromagnetic calorimetry or muon chambers, or from inefficiencies in the particle identification algorithms, a substantial fraction of $l^+l^-l'^+l'^-$ events was misidentified as having a pair of taus. The 48 events selected in the data were classified as follows: 7 in the $e^+e^-e^+e^-$ channel, 14 as $e^+e^-\mu^+\mu^-$, 16 as $e^+e^-\tau^+\tau^-$, 2 as $\mu^+\mu^-\mu^+\mu^-$, 7 as $\mu^+\mu^-\tau^+\tau^-$ and 2 as $\tau^+\tau^-\tau^+\tau^-$.

6.2 $Z\gamma^*$ production in $l^+l^-l'^+l'^-$: Results

The value of the $Z\gamma^*$ cross-section at each energy point was extracted using a procedure which followed closely that adopted for the $l^+l^-q\bar{q}$ channels in section 4.1. Bidimensional mass distributions were constructed in the plane of the masses of the pairs with the larger

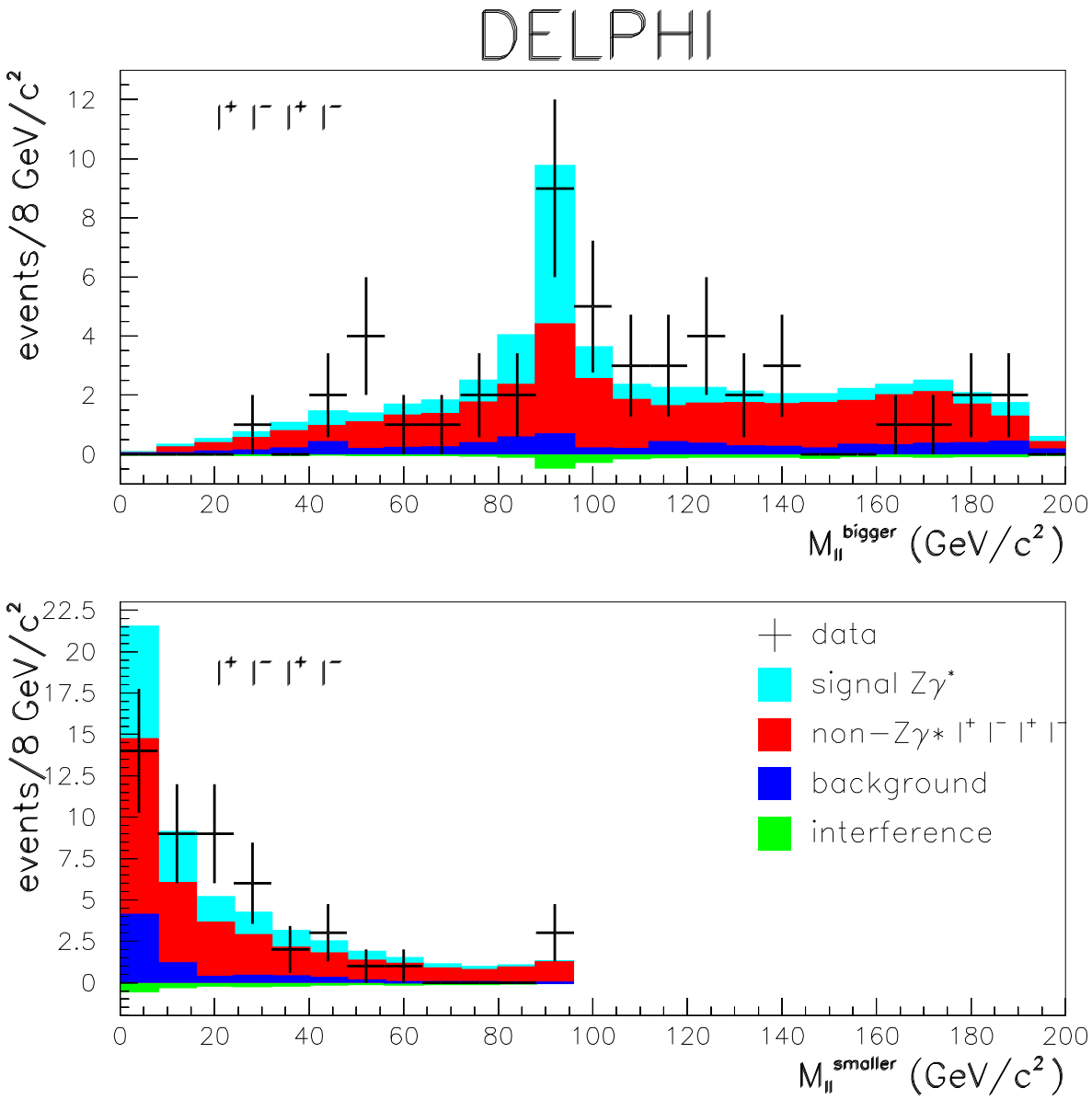

Figure 10: Four-lepton channel: Fitted masses of two selected lepton pairs: bigger mass (top plot), smaller mass (bottom plot), compared with Standard Model predictions. The points are the data, summed over all energy points, and the histograms represent the predicted contributions to the selected event sample. In the legend, "background" means the contribution from non-$l^+l^-l'^+l'^-$ final states.

and smaller mass in the event. The distributions were binned using the same definition as the first five bins in figure 4 for the $e^+e^-q\bar{q}$ case. Of the 15.1 events predicted as the $Z\gamma^*$ plus the non-$Z\gamma^*$ $l^+l^-l'^+l'^-$ contributions to the total signal, 3.2 were predicted in the $e^+e^-e^+e^-$ channel, 4.5 in $e^+e^-\mu^+\mu^-$, 3.0 in $e^+e^-\tau^+\tau^-$, 1.6 in $\mu^+\mu^-\mu^+\mu^-$, 2.2 in $\mu^+\mu^-\tau^+\tau^-$ and 0.6 in $\tau^+\tau^-\tau^+\tau^-$, while, of the 17 selected data events, 1, 4, 6, 1, 5 and 0 were assigned to each of these channels, respectively.

A one-parameter binned likelihood fit to the $Z\gamma^*$ $l^+l^-l'^+l'^-$ contribution was performed, fixing the non-$Z\gamma^*$ contribution and the remaining backgrounds and interference terms to the Standard Model expectations. These results, shown in the right side of table 5, were used to derive the combined values of the $Z\gamma^*$ cross-section in the Matrix Element signal definition, as described in section 8.

6.3 $Z\gamma^*$ production in $l^+l^-l'^+l'^-$: Systematic errors

Several sources of systematic uncertainties were investigated.

The main contribution to the systematic error in the track selection came from the difference between data and simulation in the number of reconstructed charged-particle tracks. In order to estimate this uncertainty, samples of dimuon events were generated and the numbers of events with one, two or three reconstructed charged tracks compared in data and simulation. From the comparison, a conservative uncertainty of $\pm 5\%$ was assigned as the systematic error from this source. For dimuon events with two reconstructed charged-particle tracks, the difference between data and simulation in the number of events with total charge equal to zero was found to be of the order of $+0.5\%$.

A contribution of 1.5% was added due to differences between data and simulation in the charge misidentification of electrons in the low polar angle region.

Systematic uncertainties originating from particle identification were also taken into account. Two pure samples of e^+e^- and $\mu^+\mu^-$ final states were selected from the data using particle identification criteria independent of those described in section 6.1 and were compared with simulated samples of the same final states. Then the identification criteria for electrons and muons were applied to both samples and the difference in the efficiencies between data and simulation was taken as a systematic error. This resulted in errors of $\pm 0.5\%$ for muons and $\pm 5\%$ for electrons. The poorer of the two estimates was also used for taus and adopted as a systematic uncertainty on the cross-section measurement.

Possible errors arising from the procedure adopted in the fits to the l^+l^- mass distribution were studied. Several checks were performed, in close analogy to those described in section 4.2. First, simulated samples of events with electrons in the final state (which receive large contributions from t-channel processes) were split into two categories, depending on whether or not the electrons were identified in the event reconstruction. The cross-sections of the two samples were measured and then combined. Secondly, a one-parameter fit to the mass distribution was performed, both on the whole selected $l^+l^-l'^+l'^-$ sample and on the two separated samples with final state electrons described above, allowing only the $Z\gamma^*$ component to vary. From the spread of the results of these additional fits, a systematic error of $\pm 7\%$ was estimated.

The error in the efficiency for selecting signal events due to the limited Monte Carlo statistics was evaluated to be $\pm 0.6\%$. The limited statistics available for the different background processes were also taken into account, as well as the theoretical uncertainties in the cross-sections, resulting in contributions of $\pm 0.06\%$ and $\pm 1.1\%$, respectively. Finally, a contribution to the systematic error of $\pm 0.6\%$ was estimated from the uncertainty in the measurement of the luminosity.

The total estimated systematic error on the $l^+l^-l'^+l'^-$ $Z\gamma^*$ cross-section measurement was thus estimated to be $\pm 10\%$.

6.4 Measurement of the total cross-section for $l^+l^-l'^+l'^-$ production

In this section we report a total cross-section measurement for $l^+l^-l'^+l'^-$ production, in addition to the study of $Z\gamma^*$ production in the four-lepton topology described in section 6.2 above.

As the cross-section does not vary too much within the energy range of LEP2, all the data and the Monte Carlo simulations for the different energies were grouped together. The total cross-section was then estimated from a likelihood fit to the Poissonian probability for observing the number of events found in the data, given the expected number corresponding to a total cross-section, σ, for $l^+l^-l'^+l'^-$ production, plus the estimated number of background events (see table 5).

The total cross-section for the $l^+l^-l'^+l'^-$ processes was found to be

$$\sigma = (0.430 \pm 0.072 \pm 0.023) \text{ pb}$$

within the visible region, defined by $|\cos\theta_l| \leq 0.98$, at a luminosity-averaged centre-of-mass energy of 197.1 GeV. The first error quoted is statistical; the second is the estimated systematic error, derived as described in section 6.3 above, but without including effects involving particle identification.

This result is in good agreement with the predicted cross-sections from WPHACT, which range from 0.440 pb at $\sqrt{s} = 182.7$ GeV to 0.375 pb at $\sqrt{s} = 206.5$ GeV, giving a luminosity-weighted average cross-section of 0.403 pb within the visible region at $\sqrt{s} = 197.1$ GeV.

7 Study of the $q\bar{q}q\bar{q}$ final state

The measurement of the $Z\gamma^*$ contribution in the $q\bar{q}q\bar{q}$ channel has to deal with background processes such as $q\bar{q}(\gamma)$ and WW which have cross-sections larger by orders of magnitude than the signal. It is thus not feasible to measure the $Z\gamma^*$ cross-section in all the possible $q\bar{q}$ mass spectrum. Only a restricted region was thus considered here, for low values of the reconstructed mass of one $q\bar{q}$ pair. The signature of the process studied in this analysis is the presence of a highly energetic isolated low mass jet from the γ^* hadronisation (preferentially directed in the forward region), recoiling against a system of two (or more) jets from the hadronic Z decay. The study of the γ^* system was limited to final states with only two charged particles and an arbitrary number of neutral particles; this choice was driven by the expectation that, in the low mass region, the process $\gamma^* \to q\bar{q}$ is dominated by the hadronisation chain $\gamma^* \to \rho^0 \to \pi^+\pi^-$. Furthermore, an explicit cut on the reconstructed mass of the two selected charged-particle tracks was used, as explained below. The $Z\gamma^*$ signal definition was kept the same as in the other channels studied (with no limits on the γ^* mass); as a result, the two selection criteria mentioned above (those requiring low charged-particle multiplicity and low reconstructed mass) imply a large inefficiency in the analysis of events with $\gamma^* \to q\bar{q}$ for γ^* masses above a few GeV/c^2.

The principal backgrounds arise from production of $q\bar{q}(\gamma)$, WW and final states from other four-fermion neutral current processes such as $q\bar{q}\mu^+\mu^-$, $q\bar{q}e^+e^-$ and $q\bar{q}\tau^+\tau^-$.

A pre-selection was applied to the data in order to select hadronic events compatible with the expected topologies. The total charged-particle multiplicity was required to be larger than 20; the ratio $\sqrt{s'}/\sqrt{s}$ had to be larger than 77%, where $\sqrt{s'}$ is the reconstructed effective centre-of-mass energy [23]; events with neutral particles with electromagnetic energy exceeding 50 GeV were excluded; the missing energy of the event was required to be less than 82% of the centre-of-mass energy; and the number of identified muons was required to be less than two (to limit the background from $q\bar{q}\mu^+\mu^-$ events). Events were then clustered according to the LUCLUS [20] algorithm with the parameter d_{join} set to 6.5 GeV/c, and it was required that the number of reconstructed jets in the event be larger than two. One of the jets had to contain at least one charged particle with momentum exceeding 32 GeV/c and to have charged-particle multiplicity of two, while an arbitrary number of neutral particles was accepted in the jet. The pair of charged particles was then subjected to the selections listed below:

- The impact parameters of the two charged particles were required to be compatible with production at the primary event vertex;
- The total energy of the pair was required to be larger than 63 GeV;
- The two charged particles had to be of opposite charge;
- The total energy deposited by the two particles in the electromagnetic calorimeters was required to be less than 40% of the total energy of the pair;
- Identified muons and electrons (soft identification criteria, see section 4) were not allowed in the pair;
- The system recoiling against the jet containing the selected pair was forced into a two-jet configuration and the full kinematics of the three jets was completely determined by their space directions. Then the two-jet system not containing the selected pair was required to have a reconstructed mass within 11 GeV/c^2 of the nominal Z mass;
- The invariant mass of the two charged particles had to be less than 2.1 GeV/c^2.

Numerical values of the cuts were optimised by scanning the full range of the relevant discriminating variables and calculating, for each set of values, the cross-section and the product of the efficiency and purity of the selected sample. The set with the highest value of the product of efficiency, ϵ, and purity, p, corresponding to $\epsilon = 2.2\%$ and $p = 69.6\%$, was chosen, yielding a ratio $\frac{signal}{\sqrt{background}} = 3.3$. The procedure selected 7 events in data and 6.9 in the simulation, of which 4.8 were signal and 2.1 were background. The main backgrounds came from WW (1.1 events), $q\bar{q}(\gamma)$ (0.4 events) and other four-fermion neutral current processes (0.4 events). Figure 11 compares the distribution of the reconstructed mass of the pair of selected charged-particle tracks before the last cut with Standard Model predictions. Table 7 shows the predicted numbers of signal and background events and the observed numbers of events in the $q\bar{q}q\bar{q}$ channel at the various centre-of-mass energies.

The value of the $Z\gamma^*$ cross-section at each energy point was extracted using a counting technique and the values were then combined to determine a global result. All non-$Z\gamma^*$ contributions, backgrounds and interference terms were fixed to the Standard Model expectations. The results were used to derive a combined value for the $Z\gamma^*$ cross-section for the Matrix Element signal definition, as described in section 8.

7.1 Systematic errors

Various sources of systematic error were considered.

E (GeV)	Data	Total MC	Signal	Background
182.7	1	0.4	0.4	0.1
188.6	2	1.9	1.4	0.5
191.6	0	0.2	0.2	0.0
195.5	0	0.8	0.4	0.4
199.5	0	1.0	0.8	0.2
201.6	2	0.3	0.2	0.0
205.0	1	0.6	0.4	0.2
206.5	1	1.7	1.0	0.7
Total	7	6.9	4.8	2.1

Table 7: Observed numbers of events in the $q\bar{q}q\bar{q}$ channel at each energy compared with the Standard Model predictions for signal and background.

The predicted background contributions from WW, $q\bar{q}(\gamma)$ and four-fermion neutral current production were varied by changing the cross-sections for these processes according to the values given in section 5.5: the combined effect on the cross-section measurement was estimated to amount to $\pm 0.8\%$.

The statistical error corresponding to the limited simulated sample gave an uncertainty of $\pm 8\%$.

The reliability of the simulation in reproducing the amount of background was checked by repeating the analysis, selecting pairs of particles of the same charge. The same cuts as those described in section 7 were applied, with the exclusion of the requirement on the total charge of the pair. No events were selected in data, while 0.56 were predicted by the simulation. The results are of course compatible, but to derive a numerical estimate for a systematic error, the procedure was modified so as to select a larger number of events: the cut on the invariant mass of the pair of charged-particle tracks - made at 2.1 GeV/c^2 in the main analysis - was increased to 10 GeV/c^2. All the other selections were left unchanged. This gave 3 events in data and 4.5 in the simulation, of which 3.6 were due to WW production and 0.5 to $q\bar{q}(\gamma)$ backgrounds.

A similar study was performed to check the four-fermion neutral current background, which gave a negligible contribution in the previous procedure. The selections in section 7 were repeated on data and simulation, but replacing the veto on identified electrons or muons in the selected pair of charged tracks by the requirement that at least one of the two tracks was positively identified as a lepton (electron or muon). In addition, the cut on the invariant mass of the pair was softened to 10 GeV/c^2, as for the check described in the previous paragraph. This resulted in 8 events selected in the data and 6.9 predicted from the simulation, of which 5.7 were due to the four-fermion neutral current background (in particular $l^+l^-q\bar{q}$ events, with $l \equiv e, \mu, \tau$) and 0.9 from the WW background.

As the two last procedures (requirement on the total charge of the pair and on the presence of leptons in the pair) each showed good agreement between data and the predictions of the simulation, the results were summed, and the larger of the statistical error of the data and the difference between data and simulation was assumed as a systematic uncertainty. This was estimated to be $\pm 13\%$ on the cross-section measurement.

The uncertainty on the cross-section measurement due to the measurement of the luminosity was evaluated to be $\pm 0.6\%$.

Finally, the stability of the result as a function of the applied experimental cuts was checked by varying the numerical values of the analysis selections. The procedure set

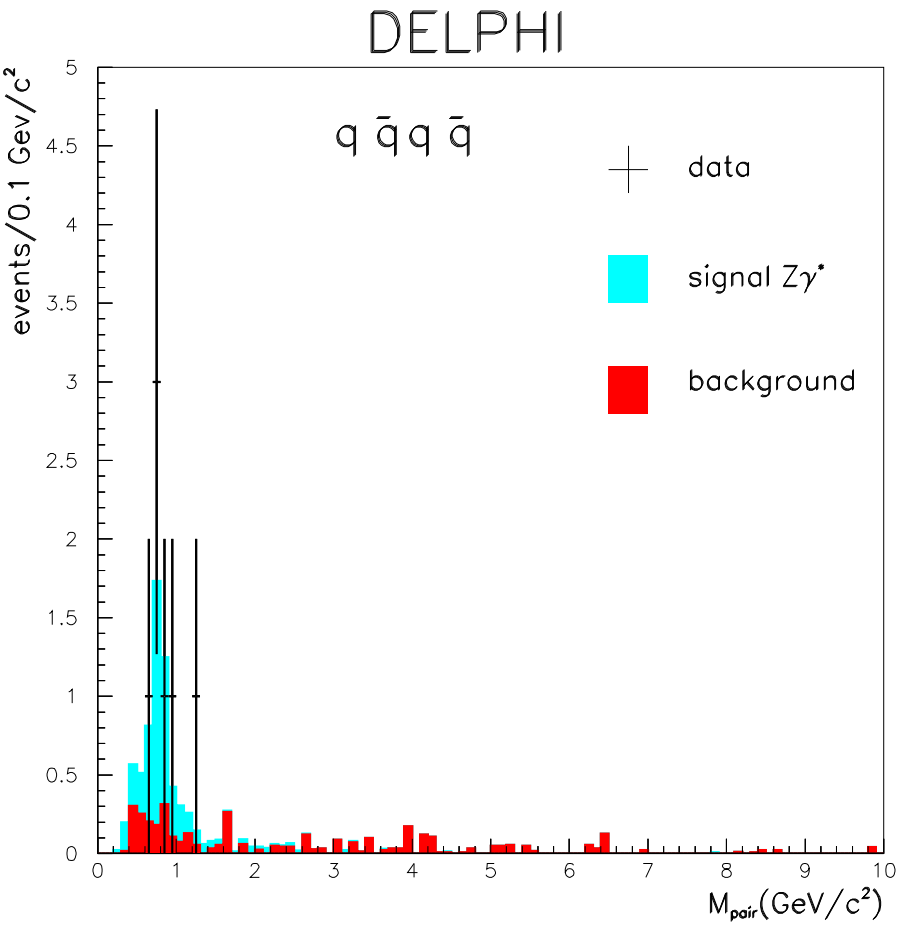

Figure 11: The distribution of the reconstructed invariant mass of the selected pair of charged-particle tracks in the $q\bar{q}q\bar{q}$ analysis, compared with the predictions of the Standard Model. The points are the data, summed over all energy points and shown before the final selection of $M_{pair} < 2.1$ GeV/c^2; the light (blue) histogram shows the predicted $Z\gamma^*$ contribution, and the dark (red) histogram shows the predicted background.

up to maximise the product of the efficiency and purity of the simulated sample (see section 7) was used to vary all the relevant cuts within reasonable limits; selections were accepted if the predicted product of the efficiency and purity of the sample differed by less than the statistical error of the simulated sample from the optimum value used in the analysis. For each new selection, the signal efficiency, background level and number of events in data were estimated, and a value for the cross-section was measured. The root mean square of the distribution of the cross-sections thus obtained was evaluated to be 15% of the central value. As this number is compatible with the statistical fluctuations intrinsic to this procedure, no systematic error was added.

The total estimated systematic error on the $q\bar{q}q\bar{q}$ $Z\gamma^*$ cross-section measurement was thus estimated to be $\pm 15\%$.

8 Results

The measurements described in the previous sections all show good agreement with the expectations of the Standard Model. In this section, we use these measurements to give results for the ratio, $R_{Z\gamma^*}$, of the measured to the expected $Z\gamma^*$ cross-section, for each of the final states considered, for their combination at each of the LEP energy points at which data were taken, and for the overall average. All these results are given in terms of the Matrix Element signal definition (see section 2). Results for the LEP signal definition are given in section 9.

Individual cross-sections were extracted by maximising probability functions with respect to the value of the $Z\gamma^*$ cross-section: Poissonian probabilities, based on the number of events selected in data and predicted in the simulation, were used for the $q\bar{q}\nu\bar{\nu}$ and $q\bar{q}q\bar{q}$ channels; probability functions derived from fitting procedures were used for the $\mu^+\mu^- q\bar{q}$, $e^+e^- q\bar{q}$ and $l^+l^-l'^+l'^-$channels. For each centre-of-mass energy, results were expressed in terms of the ratio $R_{Z\gamma^*}$ of measured to expected cross-sections, thus automatically taking into account the (smooth) dependence with energy predicted by the Standard Model. The results obtained for the different energies were first combined for each channel separately, and then into a single value. Global likelihoods were constructed to perform such combinations. The central value was defined as the point of minimum $-\log L$ distribution and the statistical error as the interval around the central value which contained 68.27% of the probability. The results obtained for the different channels are shown in table 8 and in figure 12. The table also shows the average cross-section predicted by the Standard Model for each of the final states considered at the luminosity-weighted average centre-of-mass energy of 197.1 GeV.

Table 9 compares the results at the various energy points, averaged over the different channels, with the Standard Model predictions, and this comparison is also shown in figure 13.

The systematic uncertainties for each channel were studied by introducing appropriately modified assumptions for backgrounds and efficiencies (as described in the corresponding sections) and were considered as fully correlated between the energies. The effect of systematic uncertainties in the combination of different channels was taken into account considering the uncertainties due to the luminosity measurement and to variations in the predicted background cross-sections as correlated between the channels, and all other effects as uncorrelated.

The final result is

$$R_{Z\gamma^*} \;=\; 1.04\;^{+0.13}_{-0.12}(stat)\;\pm\;0.04(syst)$$

for $|\cos\theta_{f^\pm}| < 0.98$, as shown in tables 8 and 9 and in figure 12. This result is in good agreement with the Standard Model expectation.

9 Analyses and Results for the LEP signal definition

The analyses of the three dominant channels in the final result combination ($\mu^+\mu^- q\bar{q}$, $e^+e^- q\bar{q}$, $q\bar{q}\nu\bar{\nu}$, see table 8), described in sections 4 and 5, were repeated adopting the LEP signal definition (see section 2). Some modifications were introduced to the analyses described in the sections referred to above, in order to take into account the fact that

channel	$R_{Z\gamma^*}$	σ (pb)	$\bar{\sigma}_{SM}$ (pb)
$\mu^+\mu^- q\bar{q}$	$0.98^{+0.21}_{-0.19} \pm 0.05$	$0.108^{+0.023}_{-0.021} \pm 0.005$	0.11
$e^+e^- q\bar{q}$	$1.05^{+0.32}_{-0.30} \pm 0.06$	$0.115^{+0.035}_{-0.033} \pm 0.007$	0.11
$q\bar{q}\nu\bar{\nu}$	$1.05^{+0.22}_{-0.21} \pm 0.08$	$0.084^{+0.018}_{-0.017} \pm 0.006$	0.08
$l^+l^-l'^+l'^-$	$1.31^{+0.52}_{-0.44} \pm 0.13$	$0.039^{+0.016}_{-0.013} \pm 0.004$	0.03
$q\bar{q}q\bar{q}$	$1.09^{+0.60}_{-0.47} \pm 0.16$	$0.316^{+0.174}_{-0.136} \pm 0.047$	0.29
Total	$1.04^{+0.13}_{-0.12} \pm 0.04$	$0.666^{+0.083}_{-0.077} \pm 0.026$	0.64

Table 8: Ratios of measured to predicted cross-sections and measured cross-sections for individual channels contributing to the $Z\gamma^*$ process, using the Matrix Element signal definition (see section 2). The first errors are statistical and the second systematic. In the last column $\bar{\sigma}_{SM}$(pb) is the average, luminosity-weighted $Z\gamma^*$ cross-section predicted by the Standard Model at the average energy of 197.1 GeV.

E (GeV)	$R_{Z\gamma^*}$	σ (pb)	σ_{SM} (pb)
182.7	$1.55^{+0.54}_{-0.46} \pm 0.04$	$1.15^{+0.40}_{-0.34} \pm 0.03$	0.74
188.6	$0.83^{+0.27}_{-0.23} \pm 0.04$	$0.57^{+0.19}_{-0.16} \pm 0.03$	0.69
191.6	$0.41^{+0.58}_{-0.17} \pm 0.04$	$0.27^{+0.39}_{-0.11} \pm 0.03$	0.67
195.5	$1.18^{+0.47}_{-0.39} \pm 0.04$	$0.78^{+0.31}_{-0.26} \pm 0.03$	0.66
199.5	$0.89^{+0.43}_{-0.35} \pm 0.04$	$0.58^{+0.28}_{-0.23} \pm 0.03$	0.65
201.6	$2.63^{+0.88}_{-0.74} \pm 0.04$	$1.66^{+0.55}_{-0.47} \pm 0.03$	0.63
205.0	$1.52^{+0.56}_{-0.49} \pm 0.04$	$0.90^{+0.33}_{-0.29} \pm 0.02$	0.59
206.5	$0.44^{+0.24}_{-0.20} \pm 0.04$	$0.25^{+0.14}_{-0.11} \pm 0.02$	0.57
Average	$1.04^{+0.13}_{-0.12} \pm 0.04$	$0.67^{+0.08}_{-0.08} \pm 0.03$	0.64

Table 9: Ratios of measured to predicted cross-sections and measured cross-sections averaged over the different channels at the various energy points, using the Matrix Element signal definition (see section 2). The first errors are statistical and the second systematic. The last column shows the Standard Model predictions, and the entries in the last row refer to the luminosity-averaged centre-of-mass energy of 197.1 GeV.

the di-fermion invariant mass regions below the cuts described in section 2 must now be considered as background.

- In the $l^+l^-q\bar{q}$ analysis two additional selections were introduced with respect to those described in section 4: it was required that the reconstructed mass, $M_{l^+l^-}$, of the two charged leptons be larger than 4 GeV/c^2 and that the reconstructed mass of the remaining hadronic system be larger than 8 GeV/c^2. This corresponds to reducing the content of bin 1 in the plots of figures 4, 5 and 6 and of bin 4 for muons and bin 6 for electrons in the same figures. The other steps of the analysis were left unchanged and the same procedures were applied to evaluate the systematic errors. The total systematic uncertainty on the measured $Z\gamma^*$ cross-section with the LEP signal definition was estimated to be $\pm 6\%$ for $\mu^+\mu^-q\bar{q}$ and $\pm 7\%$ for $e^+e^-q\bar{q}$.
- In the $q\bar{q}\nu\bar{\nu}$ analysis similar modifications were introduced. The low mass analysis (see section 5.1) was not used, while in the energy asymmetry and high mass analyses (see sections 5.2 and 5.3, respectively), it was required that the reconstructed mass

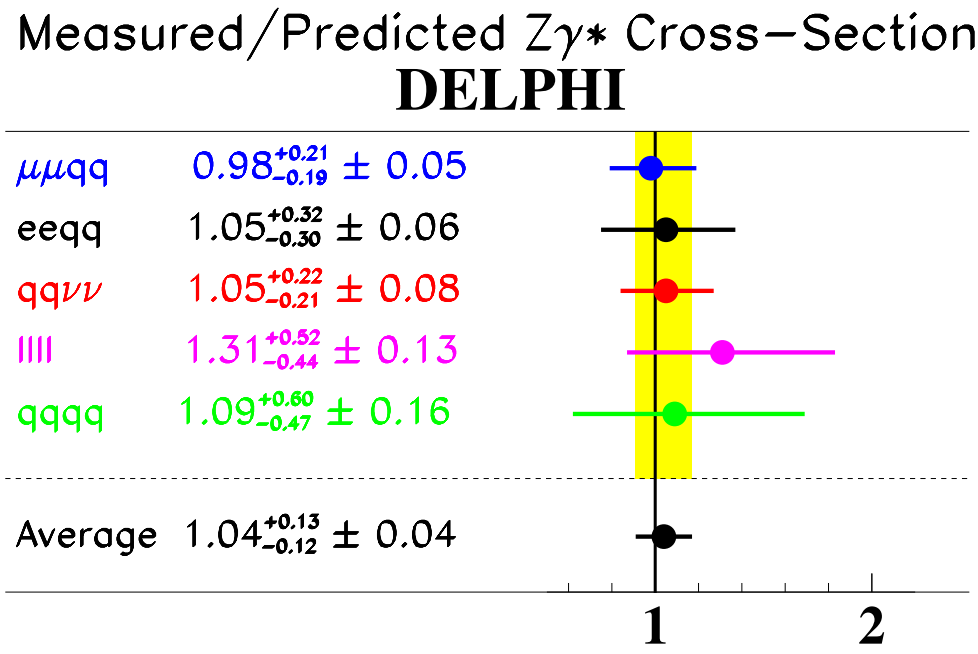

Figure 12: Ratios of measured to predicted cross-sections for individual channels contributing to the $Z\gamma^*$ process, using the Matrix Element signal definition (see section 2). The vertical band displays the total error on the combination of the channels.

of the hadronic system be larger than 8 GeV/c^2. The other steps of the analyses were left unchanged and the same procedures were applied to evaluate the systematic errors. The total systematic uncertainty on the measured $Z\gamma^*$ cross-section with the LEP signal definition was estimated to be ±16%.

The same procedures as described in section 8 were applied in order to obtain results for the $Z\gamma^*$ cross-sections with the LEP signal definition. The final results for the three channels used are summarised in table 10. A combined value of

$$\sigma_{Z\gamma^*} \;=\; 0.136\ ^{+0.029}_{-0.027}(stat) \;\pm\; 0.008(syst)\ \text{pb}$$

was obtained for the luminosity-weighted cross-section with the LEP signal definition, in good agreement with the Standard Model prediction of 0.151 pb.

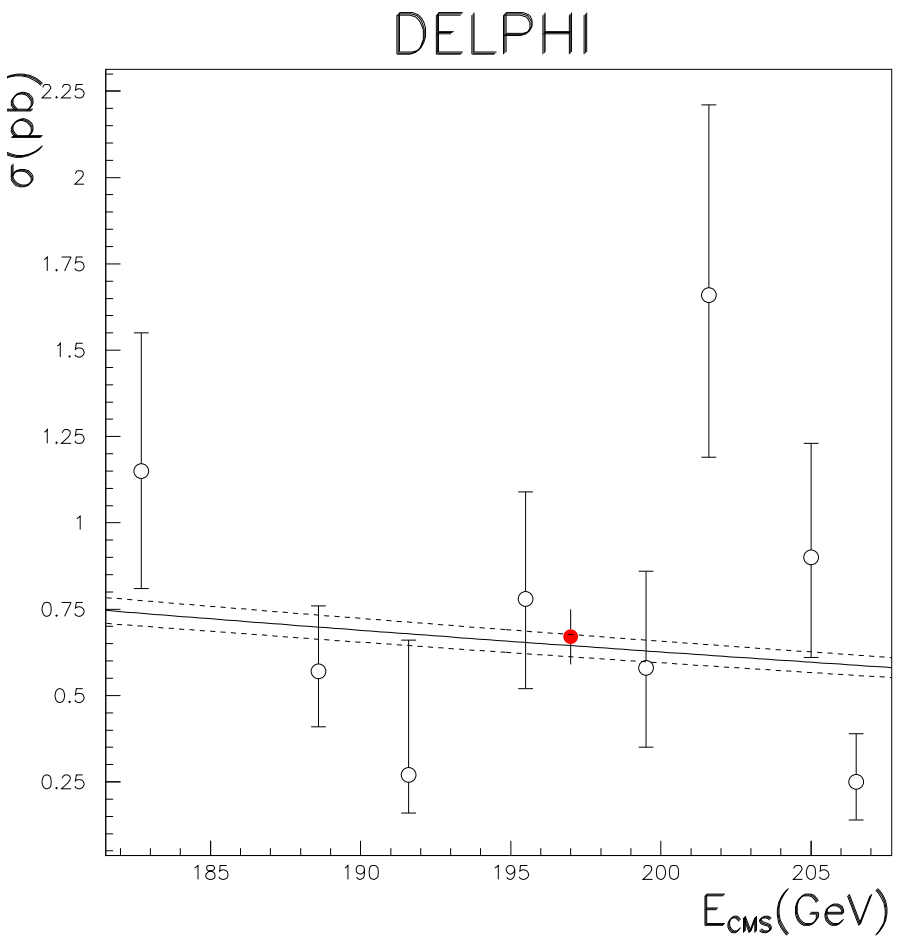

Figure 13: Combined $Z\gamma^*$ cross-section as a function of the centre-of-mass energy, using the Matrix Element signal definition (see section 2). The solid line is the Standard Model prediction; the dashed line represents a 5% uncertainty around this prediction. The full (red) point is the average cross-section result, plotted at the luminosity-weighted average centre-of-mass energy.

10 Conclusions

In the data sample collected by the DELPHI detector at centre-of-mass energies ranging from 183 GeV to 209 GeV, the values of the $Z\gamma^*$ cross-section contributing to the four-fermion final states $\mu^+\mu^- q\bar{q}$, $e^+e^- q\bar{q}$, $q\bar{q}\nu\bar{\nu}$, $l^+l^-l^+l^-$ and $q\bar{q}q\bar{q}$ with $|\cos\theta_{f^\pm}| < 0.98$ have been measured and compared with Standard Model expectations. A combined value of

$$R_{Z\gamma^*} \;=\; 1.04\ ^{+0.13}_{-0.12}(stat) \;\pm\; 0.04(syst)$$

was obtained for the ratio of the measured to the predicted cross-section in the Matrix Element signal definition (described in section 2). This corresponds to a luminosity-weighted measured cross-section of

$$\sigma_{Z\gamma^*} \;=\; 0.666\ ^{+0.083}_{-0.077}(stat) \;\pm\; 0.026(syst)\ \text{pb}\ ,$$

in good agreement with the value of 0.640 pb predicted by the Standard Model.

channel	$R_{Z\gamma^*}$	σ (pb)	$\bar{\sigma}_{SM}$ (pb)
$\mu^+\mu^- q\bar{q}$	$0.74^{+0.30}_{-0.26} \pm 0.05$	$0.031^{+0.013}_{-0.011} \pm 0.002$	0.042
$e^+e^- q\bar{q}$	$1.05^{+0.30}_{-0.29} \pm 0.08$	$0.061^{+0.017}_{-0.017} \pm 0.004$	0.058
$q\bar{q}\nu\bar{\nu}$	$0.83^{+0.44}_{-0.27} \pm 0.13$	$0.042^{+0.022}_{-0.014} \pm 0.007$	0.051
Total	$0.90^{+0.19}_{-0.18} \pm 0.05$	$0.136^{+0.029}_{-0.027} \pm 0.008$	0.151

Table 10: Ratios of measured to predicted cross-sections and luminosity-weighted cross-sections for individual channels contributing to the $Z\gamma^*$ process, using the LEP signal definition (see section 2). The first errors are statistical and the second systematic. In the last column $\bar{\sigma}_{SM}$(pb) is the average, luminosity-weighted $Z\gamma^*$ cross-section predicted by the Standard Model.

Additional cross-section measurements in the channels $\mu^+\mu^- q\bar{q}$, $e^+e^- q\bar{q}$ and $q\bar{q}\nu\bar{\nu}$ were performed using the common LEP signal definition (also described in section 2). A combined, luminosity-weighted, value of

$$\sigma_{Z\gamma^*} \;=\; 0.136\ ^{+0.029}_{-0.027}(stat) \;\pm\; 0.008(syst)\ \text{pb}$$

was obtained, in good agreement with the Standard Model prediction of 0.151 pb.

Acknowledgements

We are greatly indebted to our technical collaborators, to the members of the CERN-SL Division for the excellent performance of the LEP collider, and to the funding agencies for their support in building and operating the DELPHI detector.
We acknowledge in particular the support of
Austrian Federal Ministry of Education, Science and Culture, GZ 616.364/2-III/2a/98,
FNRS–FWO, Flanders Institute to encourage scientific and technological research in the industry (IWT) and Belgian Federal Office for Scientific, Technical and Cultural affairs (OSTC), Belgium,
FINEP, CNPq, CAPES, FUJB and FAPERJ, Brazil,
Ministry of Education of the Czech Republic, project LC527,
Academy of Sciences of the Czech Republic, project AV0Z10100502,
Commission of the European Communities (DG XII),
Direction des Sciences de la Matière, CEA, France,
Bundesministerium für Bildung, Wissenschaft, Forschung und Technologie, Germany,
General Secretariat for Research and Technology, Greece,
National Science Foundation (NWO) and Foundation for Research on Matter (FOM), The Netherlands,
Norwegian Research Council,
State Committee for Scientific Research, Poland, SPUB-M/CERN/PO3/DZ296/2000, SPUB-M/CERN/PO3/DZ297/2000, 2P03B 104 19 and 2P03B 69 23(2002-2004)
FCT - Fundação para a Ciência e Tecnologia, Portugal,
Vedecka grantova agentura MS SR, Slovakia, Nr. 95/5195/134,
Ministry of Science and Technology of the Republic of Slovenia,
CICYT, Spain, AEN99-0950 and AEN99-0761,
The Swedish Research Council,
Particle Physics and Astronomy Research Council, UK,

Department of Energy, USA, DE-FG02-01ER41155,
EEC RTN contract HPRN-CT-00292-2002.

References

[1] K. Hagiwara, R.D. Peccei, D. Zeppenfeld and K.Hikasa, Nucl. Phys. **B282** (1987) 253.

[2] ALEPH Collaboration, A. Heister *et al.*, Eur. Phys. J. **C38** (2004) 147;
DELPHI Collaboration, J. Abdallah *et al.*, Eur. Phys. J. **C34** (2004) 127;
L3 Collaboration, P. Achard *et al.*, Phys. Lett. **B600** (2004) 22;
OPAL Collaboration, G. Abbiendi *et al.*, Phys. Lett. **B493** (2000) 249.

[3] DELPHI Collaboration, J. Abdallah *et al.*, Eur. Phys. J. **C30** (2003) 447.

[4] ALEPH Collaboration, R. Barate *et al.*, Phys. Lett. **B469** (1999) 287;
L3 Collaboration, P. Achard *et al.*, Phys. Lett. **B572** (2003) 133;
OPAL Collaboration, G. Abbiendi *et al.*, Eur. Phys. J. **C32** (2004) 303.

[5] OPAL Collaboration, G. Abbiendi *et al.*, Phys. Lett. **B544** (2002) 259;
L3 Collaboration, P. Achard *et al.*, Phys. Lett. **B616** (2005) 159.

[6] DELPHI Collaboration, P. Aarnio *et al.*, Nucl. Instr. and Meth. **A303** (1991) 233.

[7] DELPHI Collaboration, P. Abreu *et al.*, Nucl. Instr. and Meth. **A378** (1996) 57.

[8] DELPHI Silicon Tracker Group, P. Chochula *et al.*, Nucl. Instr. and Meth. **A412** (1998) 304.

[9] E. Accomando and A. Ballestrero, Comp. Phys. Comm. **99** (1997) 270;
E. Accomando, A. Ballestrero and E. Maina, Comp. Phys. Comm. **150** (2003) 166.

[10] A. Ballestrero, R. Chierici, F. Cossutti and E. Migliore, Comp. Phys. Comm. **152** (2003) 175.

[11] T. Sjöstrand *et al.*, Comp. Phys. Comm. **135** (2001) 238.

[12] S. Jadach *et al.*, Phys. Lett. **B417** (1998) 326;
W. Beenakker, F.A. Berends and A.P. Chapovski, Nucl. Phys. **B548** (1999) 3.

[13] A. Denner, S. Dittmaier, M. Roth and D. Wackeroth, Nucl. Phys. **B587** (2000) 67.

[14] S. Jadach *et al.*, Comp. Phys. Comm. **140** (2001) 432.

[15] Y. Kurihara, J. Fujimoto, T. Munehisa and Y. Shimizu, Prog. Theor. Phys. **96** (1996) 1223.

[16] M. Boonekamp, DAPNIA-SPP-01-16, hep-ph/0111213 (2001).

[17] S. Jadach, B.F.L. Ward and Z. Was, Comp. Phys. Comm. **130** (2000) 260.

[18] S. Jadach, W. Placzek and B.F.L. Ward, Phys. Lett. **B390** (1997) 298.

[19] F.A. Berends, P.H. Daverveldt and R. Kleiss, Comp. Phys. Comm. **40** (1986) 271, 285, 309.

[20] T. Sjöstrand, `PYTHIA 5.7` *and* `JETSET 7.4`, CERN-TH/7112/93 (1993);
hep-ph/9508391 (1995).

[21] F.A. Berends, R. Pittau and R. Kleiss, Comp. Phys. Comm. **85** (1995) 437.

[22] Delphi Trigger Group, A. Augustinus *et al.*, Nucl. Instr. and Meth. **A515** (2003) 782.

[23] P. Abreu *et al.*, Nucl. Instr. and Meth. **A427** (1999) 487.